Gray, W. R., Wills, R. C. J., Rae, J. W. B., Burke, A., Ivanovic, R. F., Roberts, W. H. G., et al. (2020). Wind-driven evolution of the North Pacific subpolar gyre over the last deglaciation. Geophysical Research Letters, 47, e2019GL086328. https://doi.org/10.1029/2019GL086328

Wind-driven evolution of the North Pacific subpolar gyre over the last deglaciation

William R Gray[1,2]*, Robert CJ Wills[3], James WB Rae[2], Andrea Burke[2], Ruza F Ivanovic[4], William HG Roberts[5], David Ferreira[6], Paul J Valdes[7]

[1]Laboratoire des Sciences du Climat et de l'Environnement (LSCE/IPSL), Université Paris-Saclay, Gif-sur-Yvette, France

[2]School of Earth and Environmental Science, University of St Andrews, UK

[3]Department of Atmospheric Sciences, University of Washington, USA

[4]School of Earth & Environment, University of Leeds, UK

[5]Geography and Environmental Sciences, Northumbria University, UK

[6]Department of Meteorology, University of Reading, UK

[7]School of Geographical Sciences, University of Bristol, UK

*corresponding author: william.gray@lsce.ipsl.fr

Key points

- Planktic foraminiferal $\delta^{18}O$ data indicate that the North Pacific subpolar gyre expanded southward by ~3° during the Last Glacial Maximum
- Climate models show changes in gyre extent/strength are driven by a non-linear response of the westerlies to ice sheet albedo/topography and CO_2
- Proxy data and model simulations indicate that the gyre boundary and westerlies began to migrate northward at ~16.5 ka, during Heinrich Stadial 1

Abstract

North Pacific atmospheric and oceanic circulations are key missing pieces in our understanding of the reorganisation of the global climate system since the Last Glacial Maximum (LGM). Here, using a basin-wide compilation of planktic foraminiferal $\delta^{18}O$, we show that the North Pacific subpolar gyre extended ~3° further south during the LGM, consistent with sea surface temperature and productivity proxy data. Climate models indicate that the expansion of the subpolar gyre was associated with a substantial gyre strengthening, and that these gyre circulation changes were driven by a southward shift of the mid-latitude westerlies and increased wind-stress from the polar easterlies. Using single-forcing model runs, we show that these atmospheric circulation changes are a non-linear response to ice-sheet topography/albedo, and CO_2. Our reconstruction indicates that the gyre boundary (and thus westerly winds) began to migrate northward at ~16.5 ka, driving changes in ocean heat transport, biogeochemistry, and North American hydroclimate.

Plain language summary

Despite the North Pacific's importance in the global climate system, changes in the circulation of this region since the last ice age are poorly understood. Today, the North Pacific Ocean has distinct properties north and south of ~40°N: to the south, the warm surface waters form a circulation cell that moves clockwise (the subtropical gyre); to the north, the cold surface waters form a circulation cell that moves anti-clockwise (the subpolar gyre). This difference in surface ocean circulation north and south of ~40°N is determined by the wind patterns. Here, using a compilation of oxygen isotopes measured in the carbonate shells of fossil plankton from sediment cores across the basin, which tracks changes in the spatial pattern of temperature, we reconstruct

how the position of the boundary between the gyres changed since the last ice age. Our results show that the boundary between the gyres was shifted southward by ~3° during the last ice age; this indicates that the westerly winds were also shifted southward at this time. Using numerical simulations of the climate, we find that this ice age shift in the westerly winds is primarily due to the presence of a large ice sheet over North America.

1. Introduction

Despite the North Pacific's importance in the global climate system, the reorganisation of the atmosphere and surface ocean in this region during the Last Glacial Maximum (LGM, ~20 ka) and the last deglaciation (~10-20 ka, 'the deglaciation' from here on) remain poorly constrained. Changes in atmospheric and near-surface ocean circulation within the North Pacific are potentially important drivers of observed changes in the overturning circulation and biogeochemistry of the North Pacific during the LGM and deglaciation, suggested to play a role in regulating atmospheric CO_2 (Keigwin, 1998; Okazaki *et al.*, 2010; Rae *et al.*, 2014; Gray *et al.*, 2018). The overturning and gyre circulations are also important influences on poleward ocean heat transport.

Large changes in the hydroclimate of western North America during the LGM and the deglaciation (e.g. Oviatt et al., 1999; Nelson *et al.*, 2005; Lyle *et al.*, 2012; McGee *et al.*, 2012; Kirby *et al.*, 2013; Ibarra *et al.*, 2014) have been suggested to result from the reorganisation of North Pacific atmospheric circulation (e.g. Oster *et al.*, 2015; Wong *et al.*, 2016; Lora *et al.*, 2017; Lora, 2018), with early modelling work suggesting a southward displacement of the westerly jet with the presence of the Laurentide Ice

Sheet (Manabe & Brocolli, 1985; Bartlein et al., 1998). However, evidence for this atmospheric reorganisation has not yet been identified in marine records.

Driven by opposite signs in the climatological wind stress curl ($\nabla \times \tau$), the subtropical and subpolar gyres of the North Pacific Ocean have vastly different physical and chemical properties (Boyer *et al*., 2013; Key *et al*., 2015). The boundary between the gyres (defined as the point between the gyres at which the barotropic streamfunction [$\Psi_{\text{barotropic}}$] = 0) is determined by Sverdrup balance and occurs where $\nabla \times \tau$ integrated from the eastern boundary of the basin is zero (Sverdrup, 1947; Deser *et al*., 1999). Today, the gyre boundary (which broadly determines the position of the subarctic front) is nearly zonal and lies at ~40 °N, approximately following the local $\nabla \times \tau = 0$ line. South of ~40°N, anticyclonic wind stress curl in the subtropical gyre (STG) results in surface convergence and Ekman pumping (downwelling), allowing warm, nutrient-poor, surface waters to accumulate. North of ~40°N, cyclonic wind stress curl in the subpolar gyre (SPG) results in surface divergence and Ekman suction (upwelling), bringing cold, nutrient-rich, waters from the oceans interior to the surface. Surface ocean chlorophyll concentrations are an order of magnitude higher in the SPG than in the STG. The gyre circulation also dominates ocean heat transport in the Pacific (Forget and Ferreira, 2019). The relative extent and the strength of the gyres therefore exerts a large influence over basin-wide ecology, biogeochemistry, and climate.

Coupled climate models predict a ~60% increase in wind stress curl within the subpolar North Pacific under glacial forcings compared to pre-industrial forcings (Gray *et al*., 2018). By Sverdrup balance (Sverdrup, 1947), this should result in a large and predictable response in the gyre circulation. Despite some early work suggesting the subarctic front may have shifted southward during glacial times (Thompson and Shackleton, 1980; Sawada and Handa, 1998), little is known about gyre circulation over the deglaciation. Here, we use meridional profiles of planktic foraminiferal $\delta^{18}O$ to reconstruct the position of the gyre boundary over the deglaciation. Given the relatively simple dynamical link between gyre circulation and wind stress, our gyre boundary reconstruction also helps constrain the deglacial reorganisation of the atmospheric circulation. We use an ensemble of climate models forced by a range of boundary conditions to further explore the causes and implications of our gyre boundary reconstruction for the atmospheric and near-surface ocean circulations within the North Pacific.

2. Methods

2.1 $\delta^{18}O$ as a tracer of gyre circulation

The $\delta^{18}O$ of planktic foraminiferal calcite ($\delta^{18}O_{calcite}$) is a function of both the $\delta^{18}O$ of seawater ($\delta^{18}O_{water}$) and temperature dependent fractionation ($\delta^{18}O_{calcite-water}$; supporting information), however at the basin-scale the effect of temperature is far greater than the effect of $\delta^{18}O_{water}$. The large (~20 °C) sea-surface temperature (SST) difference between the gyres (Boyer *et al.*, 2013) drives a calcite-water fractionation that is ~5.5 ‰ greater in the SPG than the STG (Figure 1d; supporting information). Therefore, although the $\delta^{18}O$ of seawater is ~1 ‰ lighter in the SPG compared to the STG due to its lower salinity (~1.5 PSU, Boyer *et al.* [2013]; Figure 1c), $\delta^{18}O_{calcite}$ is ~4.5 ‰ higher in the SPG than the STG (Figure 1e). The two gyres are thus clearly delineated in the $\delta^{18}O$ of planktic foraminiferal calcite predicted using modern temperature and $\delta^{18}O_{water}$ (Figure 1e), with the steepest meridional gradient in $\delta^{18}O_{calcite}$ at the gyre boundary (Figure 1f). The meridional profiles of SST and thus $\delta^{18}O_{calcite}$ are set by the gyre circulation (Yuan and Talley, 1996; Figure S1), allowing us to use meridional profiles of planktic foraminiferal $\delta^{18}O_{calcite}$ to identify the gyre boundary. While there are likely to be local $\delta^{18}O_{water}$ changes across the basin over the deglaciation, a salinity difference of ~12.5 PSU (using the North Pacific salinity-$\delta^{18}O_{water}$ relationship from LeGrande and Schmidt [2006]) would be required to overcome the temperature signal between the gyres. As no mechanism exists to drive such a salinity/$\delta^{18}O_{water}$ difference, temperature will always dominate the meridional pattern of $\delta^{18}O_{calcite}$ (Figure 1f) and we can use meridional profiles of $\delta^{18}O_{calcite}$ to track the position of the gyre boundary through time.

We compiled previously published planktic foraminiferal $\delta^{18}O_{calcite}$ records from near-surface dwelling species *G. ruber*, *G. bulloides*, and *N. pachyderma*, spanning the last deglaciation from the North Pacific Ocean (Figure 1; supporting information). The gyre boundary is clearly defined by the steepest meridional gradient ($\Delta\delta^{18}O_{calcite}/\Delta$Latitude) in the Holocene planktic foraminiferal $\delta^{18}O_{calcite}$ data (Figure 2; supporting information). The difference in meridional temperature gradient between the east and west of the basin is also evident in the Holocene $\delta^{18}O_{calcite}$ data, with a steeper gradient in the west of the basin (Figure 2b).

To reconstruct the position the of gyre boundary over the deglaciation, we first model the $\delta^{18}O_{calcite}$ data as a function of latitude, using a generalized additive model (GAM) in the *mgcv* package in R (Wood, 2011; Wood *et al.*, 2016; Simpson, 2018) at 100 yr timesteps from 18.5 to 10.5 ka (supporting information; Figures S2-4). The smoothing term was calculated using Restricted Maximum Likelihood (REML; Reiss, & Ogden, 2009; Wood *et al.*, 2016). We then calculate the change in gyre boundary position over the deglaciation as the latitudinal shift (x°) that minimises the Euclidean distance (L^2) between the Holocene (taken as 10.5±0.5 ka, 1σ) $\delta^{18}O_{calcite}$(Lat) GAM fit and the GAM fit at each time step, computed within a 5° latitudinal band around the maximum meridional $\delta^{18}O_{calcite}$ gradient in the Holocene data (supporting information; Figure S5). The width of this latitudinal band has a negligible effect on our results (Figure S6).

We account for the effect of whole ocean changes in sea level (i.e. $\delta^{18}O_{water}$) and SST on $\delta^{18}O_{calcite}$ by subtracting the 1‰ whole ocean change in $\delta^{18}O_{water}$ (Schrag *et al.*, 2002) and the 1.8°C global-mean change in SST (converted to $\delta^{18}O_{calcite}$ using Kim and O'Neil, 1997) from a climate model ensemble (see below), scaling the anomalies through time in proportion to the sea level curve of Lambeck et al. (2014). This scaling is most robust for $\delta^{18}O_{water}$ due to its direct correlation with global terrestrial ice volume, but the correction for global SST has very little effect (removing the correction entirely results in the reconstructed gyre boundary position being <0.5° further south during the LGM) and is not therefore a significant source of error. We opt to make this global-mean SST correction in order to minimise differences in $\delta^{18}O_{calcite}$ at different time steps relating to whole-ocean SST changes (i.e. global warming), rather than local SST anomalies from circulation. The calculated changes in gyre boundary position (ΔLat) are given in Table S2; we calculate the uncertainty in ΔLat via bootstrapping (Efron, 1979), with 10,000 realisations of the data accounting for the uncertainties in the age (±500 yrs, 1σ) and $\delta^{18}O_{calcite}$ (±0.04‰, 1σ) of the records, as well as the whole ocean change in $\delta^{18}O_{water}$ (±0.1‰, 1σ) and the global-mean change in SST (±0.6°C, 1σ) with Monte-Carlo simulation. The R code to perform the analysis is available at https://github.com/willyrgray/npac_gyres.

2.2 General circulation models

We analysed an ensemble of general circulation models forced with pre-industrial and glacial boundary conditions from the Coupled Model Intercomparison Project phase 5 (CMIP5, Taylor *et al.* 2012) and the Paleoclimate Model Intercomparison Project phase 3 (PMIP3, Braconnot *et al.* 2012; supporting information). We include all four models for which both wind stress and barotropic stream function are available in the LGM simulations (supporting information). We also analyse results from a single model (HadCM3) where LGM greenhouse gases, ice sheet topography ('green mountains'), and ice sheet albedo ('white plains') forcing were changed individually (Roberts and Valdes, 2017), as well as a series of HadCM3 runs where all forcings and boundary conditions are changed progressively over the deglaciation in 500 yr 'snapshots' (as used by Morris *et al.*, 2018), broadly following the PMIP4 protocol (see Ivanovic *et al.*, 2016 and supporting information).

3. Results and Discussion

3.1 LGM planktic foraminiferal $\delta^{18}O$, SST, and productivity

While sites that today are located well within either the modern SPG or STG display an LGM difference in $\delta^{18}O_{calcite}$ of ~1-1.5 ‰, sites located within the transition zone between the gyres display a much greater change of up to ~3 ‰ (Figure 1). This anomalously large glacial increase in $\delta^{18}O_{calcite}$ is observed in transition zone sites in the east and west of the basin. The Holocene $\delta^{18}O_{calcite}$ of sites located in today's transition zone typically falls about half-way between the $\delta^{18}O_{calcite}$ of the SPG and STG. In contrast, during the LGM the $\delta^{18}O_{calcite}$ of these same sites is almost identical to the $\delta^{18}O_{calcite}$ of sites located well within the SPG. This pattern is indicative of a southward shift in the boundary between the SPG and STG, such that sites that are located within the transition zone today were located in (or felt a much greater influence of) the SPG during the LGM.

Analysing all data from across the basin together indicates the gyre boundary was positioned 3.2° (2.2 to 4.8°, 95% CI) further south during the LGM compared with its position in the Holocene (Figure 2a). Analysing the data from east and west of 180° separately results in a smaller change in the west of 1.9° (1.4 to 2.5°, 95% CI), and a greater change in the east of 6.1° (5.1 to 7.0°, 95% CI) (Figure 2b). To assess if the larger change in the east of the basin may be an artefact of changes in coastal upwelling, a process which could also influence the local SST (and thus $\delta^{18}O_{calcite}$) anomaly, we compare the PMIP3 ensemble mean SST near the eastern boundary of the basin to the zonal mean, and zonal mean east of 180° (supporting information; Figure S10). This analysis demonstrates no anomalous cooling at the eastern margin of the basin relative to the zonal average and zonal average east of 180° in the models. A further argument against a strong influence of upwelling on the data in the east is that sites that are ~15° apart from each other latitudinally, such that they are in different upwelling regimes today and thus are likely to have undergone very different changes in upwelling since the LGM, display very similar patterns of change in $\delta^{18}O_{calcite}$ over deglaciation, with no differences in timing (Fig. 1). We note, it is more difficult to track the position of the gyre boundary in the east because of the gentler slope of the meridional temperature gradient and fewer number of sites (as reflected by the larger uncertainties in the east relative to the west). However, Sverdrup balance implies that the gyre boundary in the west of the basin should respond to the integrated wind stress curl across the entire basin; therefore, the observation of a southward shift in the gyre boundary in the west signifies a basin-wide shift in the gyre boundary, regardless of how we interpret changes in the east of the basin.

Next we look at SST and productivity proxy data to see if these other proxies qualitatively support a southward extension of the SPG during the LGM. Compiling all available Mg/Ca and $U^{k'}_{37}$ SST data (supporting information) reveals a very similar pattern of temperature changes to the foraminiferal $\delta^{18}O$ data (Figure 2c). At the LGM, the SPG shows a slight warming or no change and the STG shows a slight cooling, while transition zone sites on both the east and west of the basin show an anomalously large cooling, in agreement with a southward extension of cold subpolar waters during glacial times.

Analysing the North Pacific %Opal (a productivity proxy) compilation of Kohfeld and Chase (2011) over the last deglaciation reveals that, while the SPG and STG show a decrease in %Opal during the LGM, sites in the transition zone show a ~25% increase in %Opal on both sides of the basin (Figure 2d). This pattern is consistent with nutrient-rich subpolar waters moving further south during the LGM and increasing local productivity. The southward extension of the SPG provides a solution to the long-standing question of why, while productivity decreased throughout the SPG during LGM, it increased in the modern day location of the transition zone between the gyres (Kienast *et al.*, 2004), leading to an anti-phased pattern of productivity between the SPG and transition zone over glacial-interglacial cycles (supporting information).

3.2 LGM General Circulation Model Simulations

Every model within the PMIP3 ensemble analysed exhibits a southward shift of the gyre boundary under glacial forcings relative to pre-industrial, with an ensemble mean change of 2.7° in the zonal-mean position of $\Psi_{\text{barotropic}} = 0$ (Figures 3 and 4), in excellent agreement with our reconstruction. Consistent with the proxy data, most models show a greater shift in the east of the basin, with a model mean southward shift of 3.4°, and a smaller change in the west of 2.3° (Fig. 4c). In the models this southward shift in the southern boundary of the SPG is caused by an overall expansion of the gyre; there is no change in the location of the northern edge of the gyre, which remains at the northern boundary of the basin. In addition to the expansion of the gyre, the models show a substantial increase in gyre strength, with an ensemble mean $\Psi_{\text{barotropic}}$ increase of 8.2 Sv (maximum north of 40°N). The expansion and strengthening of the subpolar gyre circulation appear tightly coupled across all models and forcings (Figure 4b). This coupling of the expansion and strengthening of the gyre arises as both effects are driven by concurrent changes in wind stress curl, rather than through a mechanistic link based on gyre dynamics.

The PMIP3 ensemble demonstrates a 2.8° southward shift in the latitude of maximum westerly wind stress in the east of the basin, but little change in the west of the basin (Figure 3); this southward shift of the westerly winds is in keeping with early modelling work which demonstrated a southward displacement of the westerly jet during the LGM (e.g. Manabe & Brocolli, 1985; Bartlein et al., 1998; Li and Battisti, 2008). A southward shift in the position of the easterlies – such that they blow over the northern boundary of the North Pacific during the LGM, rather than over the Bering Straits and Sea as they do today (Gray *et al.*, 2018) – drives a large increase in the zonal wind stress over the subpolar gyre (50% increase in the west of the basin and 100% increase in the east of the basin). The combined effect of the increase in easterly wind stress and the southward shift and increase in westerly wind stress is a large increase in wind stress curl across the subpolar gyre (Gray *et al.*, 2018), with a southward expansion in positive wind stress curl in the east of the basin. This southward expansion in positive wind stress curl in the east drives the southward expansion of the subpolar gyre across the entire basin because the circulation is, to a good approximation, in Sverdrup balance and therefore reflects the zonal integral of $\nabla \times \tau$ from the eastern boundary of the basin (Sverdrup, 1947; Hautala *et al.*, 1994; Deser *et al.*, 1999; Wunsch, 2011).

To investigate which forcing(s) ultimately drive the wind stress and gyre circulation changes during the LGM, we analysed HadCM3 model runs with individual LGM forcings from greenhouse gases, ice sheet albedo, ice sheet topography, and combined ice sheet albedo and topography (Figure 4). Substantial changes in the wind stress and gyre circulation are only seen with the combined effects of ice sheet topography and albedo; ice sheet topography or ice sheet albedo alone have little effect, as do greenhouse gases (Figure 4; supporting information). This result illustrates a non-linearity in the response of atmospheric circulations to ice sheet forcing; this is the result of the distinct and differing seasonality in the response of the atmosphere over the Pacific to ice sheet forcing, with albedo having the greatest effect in summer and topography having the greatest effect in winter (Roberts *et al.,* 2019). Note that a further shift in the gyre boundary is seen when greenhouse gas forcing is included in addition to the ice sheet forcing (Figure 4). This shift again exceeds that expected from the sum of the individual responses, suggesting a further non-linear response to the combined ice sheet and greenhouse gas forcings (e.g. Broccoli and Manabe, 1987).

The expansion of the subpolar gyre, and associated cold waters, drives a large cooling in the mid-latitudes south of the modern-day gyre boundary. The contraction and expansion of the gyre therefore act to amplify temperature changes in the mid-latitudes over glacial-interglacial cycles. The strengthening of the SPG would increase poleward heat transport and may play a role in driving the relative warmth of the SPG during the LGM (Figure 2). A modern analogue is the Pacific Decadal Oscillation 'warm' phase, which results from a strengthening of the subpolar gyre in response to a deepening of the Aleutian Low due to stochastic fluctuations (Wills *et al.*, 2019). The gyre strengthening thus acts to dampen temperature changes in the high-latitudes over glacial-interglacial cycles.

The glacial increase in wind stress curl seen within the model ensemble would drive a large increase in Ekman suction within the subpolar gyre (Gray *et al.*, 2018). Given the close association of the wind stress curl changes driving the expansion and strengthening of the subpolar gyre, we suggest that the proxy evidence for a ~3° southward shift in the gyre boundary is also indirect evidence for a glacial increase in Ekman suction within the subpolar gyre. This increased Ekman suction helped drive a large outgassing of CO_2 from the North Pacific over deglaciation (Gray *et al.*, 2018), which likely contributed to the deglacial rise in atmospheric CO_2 (Bereiter *et al.*, 2015). Increased Ekman suction would also increase the salinity of the SPG via increased upwelling of salty subsurface waters (e.g. Warren, 1983). Furthermore, both the strengthening of the gyre circulation (via increased eddy transport from the salty STG gyre and the reduced residence time of water in the SPG; Emile-Geay *et al.*, 2003) and the reorganisation of the atmosphere (lower precipitation in the SPG due to the southward shift in the jet stream and atmospheric river events e.g. Laîné *et al.* 2009; Lora *et al.*, 2017) would increase the salinity of the SPG. The reorganisation of the atmosphere and gyre circulation in response to ice sheet forcing may therefore play an important role in pre-conditioning basin for the enhanced overturning circulation observed within the North Pacific during glacial periods (e.g. Keigwin, 1998; Matsumoto et al., 2002; Knudson and Ravelo, 2015; Max et al., 2017), and points towards a weakening of the North Pacific halocline, rather than a strengthening, under glacial climates (c.f. Haug *et al.*, 1999).

3.3 Deglaciation

Considering all of the $\delta^{18}O$ data from east and west of 180° together, our reconstruction shows the gyre boundary begins to migrate northward beginning at ~16.5 ka, during Heinrich Stadial 1 (HS1) (Fig. 5d). The boundary then appears relatively constant during the Bølling-Allerød (14.8-12.9 ka; B/A) with a second major shift north at ~12 ka, during the latter part of the Younger Dryas. There is reasonable agreement between the timing of the gyre migration in the data and the deglacial model runs, which show the majority of the change occurring between ~16.5-12 ka (Fig. 5e); however, the model shows a steady change, rather than the two-step change in the data. We speculate this is a due to the lack of routed freshwater into the North Atlantic within these model runs, via its effects on hemispheric temperature asymmetry through heat transport. The timing also agrees with evidence of lake level changes in western North America (Fig. 5c; see below) and other Pacific-wide changes in atmospheric circulation during the deglaciation (Russell *et al.*, 2014; McGee *et al.*, 2014; Jones *et al.*, 2018).

However, assessing the $\delta^{18}O$ data from the east and west of the basin separately reveals a large difference in timing; the majority of the change occurs earlier in the deglaciation in the east of the basin (~16.5-14 ka) whereas the majority of the change occurs later in the deglaciation in the west of the basin (~12.5 – 10.5 ka). This east-west difference in timing can be seen in the raw $\delta^{18}O_{calcite}$ data (Figure 1) and is too large to be explained by age model uncertainty. Contrary to the data, HadCM3 shows no difference in the timing of the northward shift of the gyre boundary between the east and west.

The northward migration of the gyre boundary in the east of the basin beginning at ~16.5 ka indicates the westerly winds in the east of the basin began to shift northward at this time, concomitant with the recession of the Laurentide Ice Sheet (Lambeck *et al.*, 2014). Such a change in atmospheric circulation within the east of the basin at this time is in good agreement with records of hydroclimate in southwestern North America (Figure 5c; Bartlein *et al.*, 1998; Lyle *et al.*, 2012; Ibarra *et al.*, 2014; McGee *et al.*, 2012; Oviatt, 2015; Lora *et al.*, 2016; Shuman & Serravezza, 2017; Bhattacharya *et al.,* 2018; McGee *et al.*, 2018), and suggests a clear role for dynamics in driving the observed changes in hydroclimate. However, given Sverdrup balance, changes in wind stress curl within the east of the basin should propagate across the basin and drive changes in the position of the gyre boundary in the west, and, as noted above, only a small change is seen in the west of the basin at this time.

One possible dynamical explanation for the observed difference in the timing between the east and west of the basin is that the jet stream became less zonal (i.e. more tilted) during this period, and as such, the northward shift in the westerlies in the east did not result in a substantial change to the integrated wind stress curl across the basin, resulting in a less zonal (i.e. more tilted) gyre. A more tilted jet stream does not seem unreasonable given the large changes in the size of the North American ice sheets beginning at this time (e.g. Lambeck *et al.*, 2014), and is in good agreement with terrestrial proxy records and paleoclimatic simulations of this time period (Wong et al., 2016; Lora et al., 2016). Increased heat transport from a more tilted gyre could help explain the anomalous warmth of the SPG during the Bølling-Allerød (e.g. Gray *et al.*, 2018), and may help drive wider northern-hemisphere warming and ice sheet collapse at this time. We note that the tilt of the gyre in the modern North Atlantic is poorly simulated by climate models (Zappa *et al.*, 2013), and thus it may also be poorly simulated in the North Pacific. We also note the other models (besides HadCM3) better simulate the larger gyre boundary shift in the east relative to the west under glacial forcing (Fig. 4c), and thus may better simulate gyre tilt.

6. Conclusions

Using a basin-wide compilation of planktic foraminiferal δ^{18}O data we show that the boundary between the North Pacific subpolar and subtropical gyres shifted southward by 3.1±0.8° (1σ) during the Last Glacial Maximum relative to the Holocene, consistent with sea surface temperature and productivity proxy data. This expansion of the North Pacific subpolar gyre is evident within all available PMIP3 climate models forced with glacial boundary conditions. The models suggest that this expansion is associated with a substantial strengthening of the subpolar gyre. The strengthening of the subpolar gyre is driven by an increase in wind stress curl within the subpolar gyre resulting from a southward shift and strengthening of the mid-latitude westerlies in the east of the basin, and a southward shift in the polar easterlies across the basin. The expansion of the gyre is driven by a southward expansion of the area of positive wind stress curl within the east of the basin, due to the southward shift in the westerlies. Using model runs with individual forcings, we demonstrate that the wind stress curl changes, and associated expansion and strengthening of the subpolar gyre, are a response to the combined effects of ice-sheet albedo, ice-sheet topography, and CO_2. Changes are small in climate model simulations where albedo, topography, and CO_2 are forced separately, compared to their combined effects, illustrating the highly non-linear nature of the response of atmospheric circulation to ice sheet forcing (e.g. Löfverström *et al*., 2014; Roberts *et al*., 2019).

The expansion and contraction of the subpolar gyre acts as a mechanism to amplify temperature changes in the mid-latitudes over glacial-interglacial cycles. On the contrary, the strengthening of the subpolar gyre would increase poleward heat transport, warming the north of the basin and dampening temperature changes in the high-latitudes over glacial-interglacial cycles. The strengthening of the gyre circulation, in conjunction with increased Ekman suction (Gray *et al*., 2018), and reduced precipitation (Lora *et al*., 2017), would also make the subpolar gyre saltier, weakening the halocline under glacial climates (c.f. Haug *et al*., 1999), and pre-conditioning the basin for enhanced overturning circulation during glacial periods (e.g. Keigwin, 1998).

Our gyre-boundary reconstruction offers a constraint on the position of the mid-latitude westerly winds over the last deglaciation and suggests the westerly winds began to shift northward at ~16.5 ka, during Heinrich Stadial 1, as the Laurentide Ice Sheet receded. This reorganisation of atmospheric circulation likely drove the large changes in hydroclimate within southwestern North America (e.g. Lora *et al*., 2016), and may be related to other changes in atmospheric circulation seen at this time across the Pacific, and throughout the tropics and Southern Hemisphere (e.g. D'Agostino et al., 2017; Jones et al., 2018).

Acknowledgments

We are grateful to Lloyd Keigwin for imparting the wisdom 'If the signal is big enough, you'll see it in the 18-O of calcite'. We thank Gavin Simpson for discussions regarding Generalized Additive Models. We acknowledge the World Climate Research Programme's Working Group on Coupled Modelling for the coordination of CMIP and thank the climate modelling groups for producing and making available their model output (https://esgf-node.llnl.gov/search/cmip5/). Insightful and constructive comments from four anonymous reviewers very much improved a previous version of this manuscript. WRG, JWBR and AB were funded Natural Environment Research Council (NERC) grant NE/N011716/1 awarded to JWBR and AB. RCJW was funded by the Tamaki Foundation, NASA (Grant NNX17AH56G), and NSF (Grant AGS-1929775). RFI was funded by a NERC Independent Research Fellowship NE/K008536/1. The planktic foraminiferal $\delta^{18}O$ compilation used in this study is available at https://doi.pangaea.de/10.1594/PANGAEA.912229 and the R code to perform the analysis is available at https://github.com/willyrgray/npac_gyres.

References

Bartlein, P.J., Anderson, K.H., Anderson, P.M., Edwards, M.E., Mock, C.J., Thompson, R.S., Webb, R.S., Webb, T., Whitlock, C, 1998. Paleoclimate simulations for North America over the past 21,000 years; features of the simulated climate and comparisons with paleoenvironmental data. Quaternary Science Reviews 17, 549-585.

Bereiter, B., S. Eggleston, J. Schmitt, C. Nehrbass-Ahles, T. F. Stocker, H. Fischer, S. Kipfstuhl, and J. Chappellaz, 2015. Revision of the EPICA Dome C CO2 record from 800 to 600 kyr before present, Geophysical Research Letters 42, doi:10.1002/2014GL061957.

Bhattacharya, T., Tierney, J.E., Addison, J.A., Murray, J.W., 2018. Ice sheet modulation of deglacial North American monsoon intensification. Nature Geoscience 11, 848-852.

Boyer, T.P., Antonov, J.I., Baranova, O.K., Coleman, C., Garcia, H.E., Grodsky, A., John- son, D.R., Locarnini, R.A., Mishonov, A.V., O'Brien, T.D., Paver, C.R., Reagan, J.R., Seidov, D., Smolyar, I.V., Zweng, M.M., 2013. World Ocean Database 2013. In: Levitus, Sydney (Ed.), Alexey Mishonov (Technical Ed.), NOAA Atlas NESDIS, vol. 72. 209 pp.

Braconnot, P., Harrison, S.P., Kageyama, M., Bartlein, P.J., Masson-Delmotte, V., Abe-Ouchi, A., Otto-Bliesner, B. and Zhao, Y., 2012. Evaluation of climate models using palaeoclimatic data. Nature Climate Change, **2**(6), 417-424.

Broccoli, A.J., Manabe, S., 1987. The influence of continental ice, atmospheric CO2, and land albedo on the climate of the last glacial maximum. Climate Dynamics **1**, 87-99.

D'Agostino, R., P. Lionello, O. Adam,and T. Schneider (2017), Factors controlling Hadley circulation changes from the Last Glacial Maximum to the end of the 21st century. Geophysical Research Letters **44**, 8585-8591. doi:10.1002/2017GL074533.

Deser, C., Alexanders, M. A., Timlin, M. S., 1999. Evidence for a Wind-Driven Intensification of the Kuroshio Current Extension from the 1970s to the 1980s. Journal of Climate **12**, 1697-1706.

Efron, B., 1979. Computers and the theory of statistics: thinking the unthinkable. SIAM Rev. **21**, 460–480. https://doi.org/10.1137/1021092.

Emile-Geay, J., Cane, M.A., Naik, N., Seager, R., Clement, A.C., van Geen, A. (2003) Warren revisited: Atmospheric freshwater fluxes and 'Why is no deep water formed in the North Pacific'. Journal of Geophysical Research **108**, doi:10.1029/2001JC001058.

Forget, G, Ferreira, D, 2019. Global ocean heat transport dominated by heat export from the tropical Pacific. *Nature Geoscience,* https://doi.org/10.1038/s41561-019-0333-7,

Gray, W.R., Rae, J.W.B, Wills, R.C.J., Shevenell, A.E., Taylor, B., Burke, A., Foster, G.L., Lear, C.H., 2018. Deglacial upwelling, productivity and CO2 outgassing in the North Pacific Ocean. Nature Geoscience **11**, 340–344.

Haug, G.H., Sigman, D.M., Tiedemann, R., Pedersen, T.F., Sarnthein M., 1999. Onset of permanent stratification in the subarctic Pacific Ocean. Nature 40, 779-782.

Hautala, S.L., Roemmich, D.H., Schmitz, W.J., 1994. Is the North Pacific in Sverdrup balance along 24°N? Journal of Geophysical Research 99, 16041-16052.

Ibarra, D. E., A. E. Egger, K. L. Weaver, C. R. Harris, and K. Maher, 2014: Rise and fall of late Pleistocene pluvial lakes in response to reduced evaporation and precipitation: Evidence from Lake Surprise, California. Geol. Soc. Amer. Bull., 126, 1387–1415, https://doi.org/10.1130/B31014.1.

Ivanovic, R.F., Gregoire, L.J., Kageyama, M., Roche, D.M., Valdes, P.J., Burke, A., Drummond, R., Peltier, W.R., Tarasov, L., 2016. Transient climate simulations of the deglaciation 21–9 thousand years before present (version 1) PMIP4 Core experiment design and boundary conditions. Geosci. Model Dev. **9**, 25632587. https://doi.org/10.5194/gmd-9-2563-2016.

Jones, T.R., Roberts, W.H.G., Steig, E.J., Cuffey, K.M., Markle, B.R., White, J.W.C (2018) Southern Hemisphere climate variability forced by Northern Hemisphere ice-sheet topography. Nature **554**, 351-355.

Keigwin, L., 1998. Glacial-age hydrography of the far northwest Pacific Ocean. Paleoceanography **13**, 323–339.

Key, R.M., Olsen, A., van Heuven, S., Lauvset, S.K., Velo, A., Lin, X., Schirnick, C., Kozyr, A., Tanhua, T., Hoppema, M., Jutterström, S., Steinfeldt, R., Jeansson, E., Ishi, M., Perez, F.F., Suzuki, T., 2015. Global Ocean Data Analysis Project, Version 2 (GLODAPv2). ORNL/CDIAC-162, ND-P093. Carbon Dioxide Informa- tion Analysis Center, Oak Ridge National Laboratory, US Department of Energy, Oak Ridge, Tennessee. https://doi.org/10.3334/CDIAC/OTG.NDP093_GLODAPv2. http://cdiac.ornl.gov/oceans/GLODAPv2/NDP_093.pdf.

Kienast, S.S., Hendy, I.L., Crusius, J., Pedersen, T.F., Calvert, S.E, 2004. Export production in the subarctic North Pacific over the last 800 kyrs: No evidence for Iron Fertilization? Journal of Oceanography 60, 189-203.

Kim, S. and O'Neil, J. (1997). Equilibrium and nonequilibrium oxygen isotope effects in synthetic carbonates. Geochimica et Cosmochimica Acta **61**, 3461–3475.

Kirby, M. E., S. J. Feakins, N. Bonuso, J. M. Fantozzi, and C. A. Hiner, 2013. Latest Pleistocene to Holocene hydroclimates from Lake Elsinore, California, Quat. Sci. Rev., 76, 1–15.

Knudson, K. P. and Ravelo, A. C., 2015. North Pacific Intermediate Water circulation enhanced by the closure of the Bering Strait. Paleoceanography **30**, PA002840.

Kohfeld, K. E. & Chase, Z., 2011. Controls on deglacial changes in biogenic fluxes in the North Pacific Ocean. Quat. Sci. Rev. **30**, 3350–3363.

Laîné, A., Kageyama, M., Salas-Mélia, D., Voldoire, A., Rivière, G., Ramstein, G., Planton, S., Tyeca, S., Peterschmitt, J.Y., 2009. Northern hemisphere storm tracks during the last glacial maximum in the PMIP2 ocean-atmosphere coupled models: energetic study, seasonal cycle, precipitation. Climate Dynamics 32, 593-614.

Lambeck, K., Rouby, H., Purcell, A., Sun, Y., Sambridge, M., 2014. Sea level and global ice volumes from the Last Glacial Maximum to the Holocene. Proc. Natl Acad. Sci. USA **111**, 15296–15303.

LeGrande, A.N., Schmidt, G.A., 2006. Global gridded data set of the oxygen isotopic composition in seawater. Geophys. Res. Lett. **33**, L12604.

Li, C., Battisti, D.S., 2008. Reduced Atlantic Storminess during Last Glacial Maximum: Evidence from a Coupled Climate Model. Journal of Climate **21** 3561-3579. DOI: 10.1175/2007JCLI2166.1.

Löfverström, M., R. Caballero, J. Nilsson, Kleman, J., 2014. Evolution of the large-scale atmospheric circulation in response to changing ice sheets over the last glacial cycle. Climate of the Past **10**, 1453-1471.

Lora, J. M., J. L. Mitchell, Tripati, A. E., 2016. Abrupt reorganization of North Pacific and western North American climate during the last deglaciation, Geophys. Res. Lett., 43, 11,796–11,804, doi:10.1002/2016GL071244.

Lora, J. M., J. L. Mitchell, C. Risi, and A. E. Tripati, 2017. North Pacific atmospheric rivers and their influence on western North America at the Last Glacial Maximum, Geophysical Research Letters 44, 1051–1059, doi:10.1002/2016GL071541.

Lora, J. M., 2018. Components and Mechanisms of Hydrologic Cycle Changes over North America at the Last Glacial Maximum. Journal of Climate 31, 7035-7051.

Lyle, M., Heusser, L., Ravelo, C., Yamamoto, M., Barron, J., Diffenbaugh, N. S., Herbert, T., Andreasen, D., 2012. Out of the Tropics: The Pacific, Great Basin Lakes, and Late Pleistocene Water Cycle in the Western United States. Science, **337**, 1629-1633.

Manabe, S., Broccoli, A.J., 1985. The influence of Continental Ice Sheets on the Climate of an Ice Age. Journal of Geophysical Research 90, 2167-2190.

Matsumoto, K., Oba, T. & Lynch-Stieglitz, J., 2002. Interior hydrography and circulation of the glacial Pacific Ocean. Quat. Sci. Rev. **21**,1693–1704.

Max, L., Rippert, N., Lembke-Jene, L., Mackensen, A., Nürnberg, D., Tiedemann, R., 2017. Evidence for enhanced convection of North Pacific Intermediate Water to the low-latitude Pacific under glacial conditions. Paleoceanography **32**, 41–55.

McGee, D., Quade, J., Edwards, R.L, Broecker, W.S., Cheng, H., Reiners, P.W., Evenson, N., 2012. Lacustrine cave carbonates: Novel archives of paleohydrologic change in the Bonneville Basin (Utah, USA). Earth and Planetary Science Letters **351-352**, 182-194.

McGee, D., Donohoe, A., Marshall, J., Ferreira, D. (2014) Changes in ITCZ location and cross-equatorial heat transport at the Last Glacial Maximum, Heinrich Stadial 1, and the mid-Holocene. Earth and Planetary Science Letters **390**, 69-79.

McGee, D., Moreno-Chamarro, E., Marshall, J., Galbraith, E.D. (2018) Western U.S. lake expansions during Heinrich stadials linked to Pacific Hadley circulation. Science Advances 4, eaav0118.

Morris, P.J., Swindles, G.T., Valdes, P.J., Ivanovic, R.F., Gregoire, L.J., Smith, M.W., Tarasov, L., Haywood, A.M., Bacon, K.L., 2018. Global peatland initiation driven by regionally asynchronous warming. PNAS 201717838. https://doi.org/10.1073/pnas.1717838115.

Nelson, S.T., Wood, M.J., Mayo, A.L., Tingey, D.G., Eggett, D., 2005. Shoreline tufa and tufaglomerate from Pleistocene Lake Bonneville, Utah, USA: stable isotopic and mineralogical records of lake conditions, processes, and climate. Journal of Quaternary Science **20**, 3–19.

Okazaki, Y., Timmermann, A., Menviel, L., Harada, N., Abe-Ouchi, A., Chikamoto, M., Mouchet, A., and Asahi, H., 2010. Deepwater Formation in the North Pacific During the Last Glacial Termination. Science **329**, 200-204.

Oster, J.L., Ibarra, D.E., Winnick, M.J., Maher, K., 2015. Steering of westerly storms over western North America at the Last Glacial Maximum. Nature Geoscience **8**, 201-205.

Oviatt, C. G., R. S. Thompson, D. S. Kaufman, J. Bright, and R. M. Forester, 1999. Reinterpretation of the Burmester Core, Bonneville Basin, Utah, Quat. Res., 52, 180–184.

Oviatt, C. G., 2015. Chronology of Lake Bonneville, 30,000 to 10,000 yr B.P. Quaternary Science Reviews 110, 166-171.

Rae, J. W. B., Sarnthein, M., Foster, G. L., Ridgwell, A., Grootes, P. M., and Elliott, T., 2014. Deep water formation in the North Pacific and deglacial CO2 rise. Paleoceanography **29**, 645–667.

Reiss, P. T., Ogden, R. T. (2009) Smoothing parameter selection for a class of semiparametric linear models. Journal of the Royal Statistical Society B **71**, 505-523.

Roberts, W. H. G., Valdes, P. J., 2017. Green Mountains and White Plains: The Effect of Northern Hemisphere Ice Sheets on the Global Energy Budget. Journal of Climate **30**, 3887- 3905. DOI: 10.1175/JCLI-D-15-0846.1.

Roberts, W.H.G., Li, C., Valdes, P.J., 2019. The mechanisms that determine the response of the Northern Hemisphere's stationary waves to North American ice sheets. Journal of Climate, https://doi.org/10.1175/JCLI-D-18-0586.1

Russell, J.M., Russell, Vogel, H., Konecky, B.L., Bijaksana, S., Huang, Y., Melles, M., Wattrus, N., Costa, K., King, J.W., 2014. Glacial forcing of central Indonesian hydroclimate since 60,000 yr BP. Proc. Natl Acad. Sci. USA 111, 5100–5105.

Sawada, K. and Handa, N., 1998. Variability of the path of the Kuroshio ocean current over the past 25,000 years. Nature **392**, 592–595.

Schrag, D. P., Adkins, J. F., McIntyre, K., Alexander, J. L., Hodell, D. A., Charles, C. D. McManus, J. F., 2002. The oxygen isotopic composition of seawater during the Last Glacial Maximum. Quaternary Science Reviews **21**, 331-342.

Shuman, B.N., Serravezza, M., 2017. Patterns of hydroclimatic change in the Rocky Mountains and surrounding regions since the last glacial maximum. Quaternary Science Reviews 173, 58-77.

Simpson, G. L., 2018. Modelling Palaeoecological Time Series Using Generalised Additive Models. Frontiers in Ecology and Evolution 6, 149. doi: 10.3389/fevo.2018.00149

Sverdrup, 1947. Wind-Driven Currents in a Baroclinic Ocean; with Application to the Equatorial Currents of the Eastern Pacific. PNAS **33**, 318–26.

Taylor, K. E., R. J. Stouffer, and G. A. Meehl, 2012: An overview of CMIP5 and the experiment design. Bull. Am. Meteorol. Soc., **93** (4), 485–498

Thompson and Shackleton, 1980. North Pacific palaeoceanography: late Quaternary coiling variations of planktonic foraminifer Neogloboquadrina pachyderma. Nature **287**, 829–833.

Warren, B.A. (1983) Why is no deep water formed in the North Pacific? Journal of Marine Research **41**, 327-347.

Wills, R. C. J., Battisti, D. S., Proistosescu, C., Thompson, L., Hartmann, D. L., & Armour, K. (2019). Ocean circulation signatures of North Pacific decadal variability. Geophysical Research Letters, 46. https://doi.org/10.1029/2018GL080716

Wong, C. I., G. L. Potter, I. P. Montañez, B. L. Otto-Bliesner, P. Behling, and

J. L. Oster (2016), Evolution of moisture transport to the western U.S. during the last deglaciation, Geophys. Res. Lett., 43, 3468–3477, doi:10.1002/2016GL068389.

Wood, S.N. (2011) Fast stable restricted maximum likelihood and marginal likelihood estimation of semiparametric generalized linear models. Journal of the Royal Statistical Society (B) **73**, 3-36.

Wunsch, C., 2011. The decadal mean ocean circulation and Sverdrup balance. Journal of Marine Research 69, 417-434.

Wood, S.N., Pya N., Säfken, B. (2016) Smoothing Parameter and Model Selection for General Smooth Models, Journal of the American Statistical Association, 111:516, 1548-1563, DOI: 10.1080/01621459.2016.1180986

Yuan, X., Talley, L.D. (1996) The subarctic frontal zone in the North Pacific: Characteristics of frontal structure from climatological data and synoptic surveys. Journal of Geophysical Research 101, 16491-16508.

Zappa, G., L.C. Shaffrey, and K.I. Hodges (2013) The Ability of CMIP5 Models to Simulate North Atlantic Extratropical Cyclones. Journal of Climate **26**, 5379–5396, https://doi.org/10.1175/JCLI-D-12-00501.1

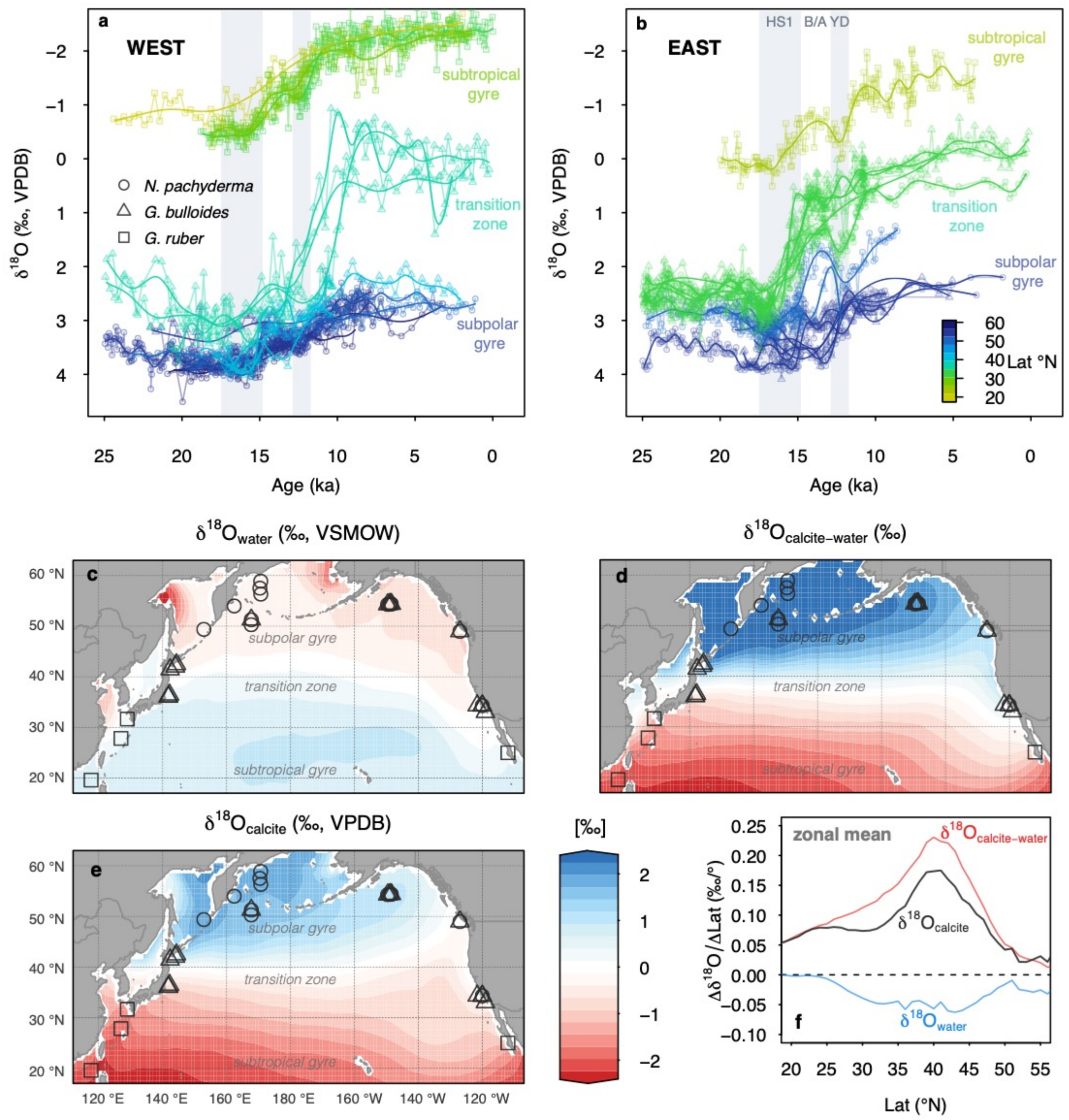

Figure 1 Planktic foraminiferal $\delta^{18}O$ versus age with core site latitude represented by colour. Data are divided east **(b)** and west **(a)** of 180°. HS1, B/A and YD are Heinrich Stadial 1 (14.8-17.5 ka), Bølling-Allerød (12.9-14.8 ka) and the Younger Dryas (11.8-12.9 ka), respectively. **(c)** gridded $\delta^{18}O_{water}$ from LeGrande and Schmidt (2006) **(d)** calcite-water fractionation calculated using WOA13 mean annual temperature (Boyer et al., 2013) and the temperature-fractionation relationship of Kim and O'Neil (1997) **(e)** predicted $\delta^{18}O_{calcite}$ using gridded $\delta^{18}O_{water}$ from LeGrande and Schmidt (2006) and calcite-water fractionation calculated using WOA13 mean annual temperature (Boyer et al., 2013) and the temperature-fractionation relationship of Kim and O'Neil (1997) (note the colour scale is the same for all three panels) **(f)** slope of the zonal-mean meridional gradient in $\delta^{18}O_{water}$, $\delta^{18}O_{calcite-water}$ and $\delta^{18}O_{calcite}$, as shown in (c), (d) and (e). The steepest part of the meridional $\delta^{18}O_{calcite}$ gradient is lies at the gyre boundary, and is a result of the large temperature difference between the gyres.

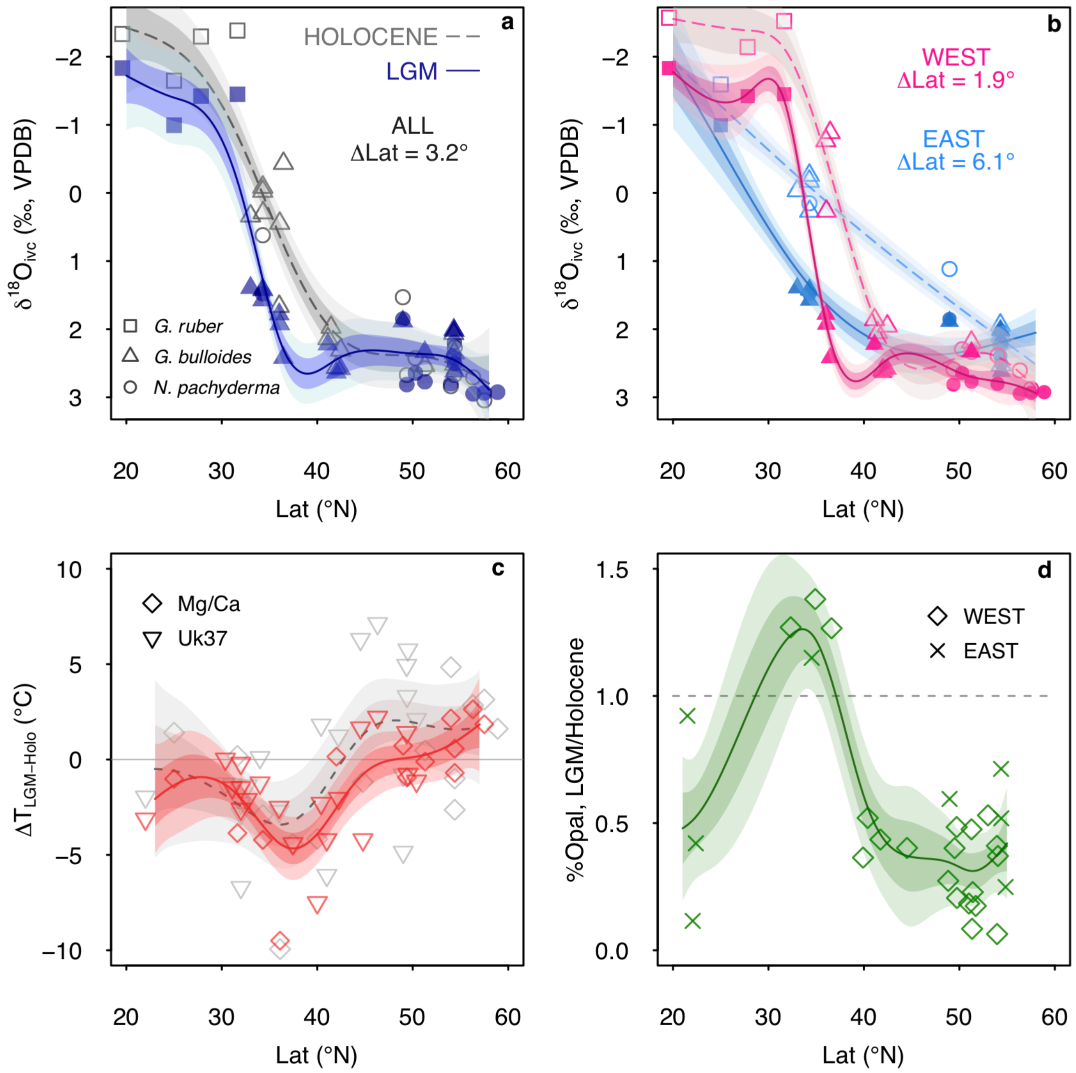

Figure 2 **(a)** Holocene (10.5 ka, open symbols, dashed line) and LGM (18.5 ka, filled symbols, solid line) foraminiferal δ^{18}O data versus latitude – symbols reflect species of planktic foraminifera (see panel a). Foraminiferal δ^{18}O values have been corrected for whole ocean changes in $\delta^{18}O_{water}$ due to changes in terrestrial ice volume and the mean ocean change in SST from the PMIP3 ensemble ($\delta^{18}O_{ivc}$; see Methods). The data are fit with a generalized additive model (see Methods), with the 68% and 95% Bayesian credible intervals shown **(b)** as in (a), however with data separated east and west of 180° **(c)** Compiled LGM-Holocene SST differences versus latitude, based on Mg/Ca and $U^{k'}_{37}$: Grey/dashed line is LGM proxy SST minus modern climatological SST. Red/solid line is LGM proxy SST minus Holocene proxy SST **(d)** Compiled %Opal (a productivity proxy) from Kohfeld and Chase (2011) data (supporting information), shown as a ratio of LGM/Holocene versus latitude, with a value of greater than 1 indicating a glacial increase. In (c) and (d) the data are fit with a generalized additive model, with the 68% and 95% Bayesian credible intervals shown.

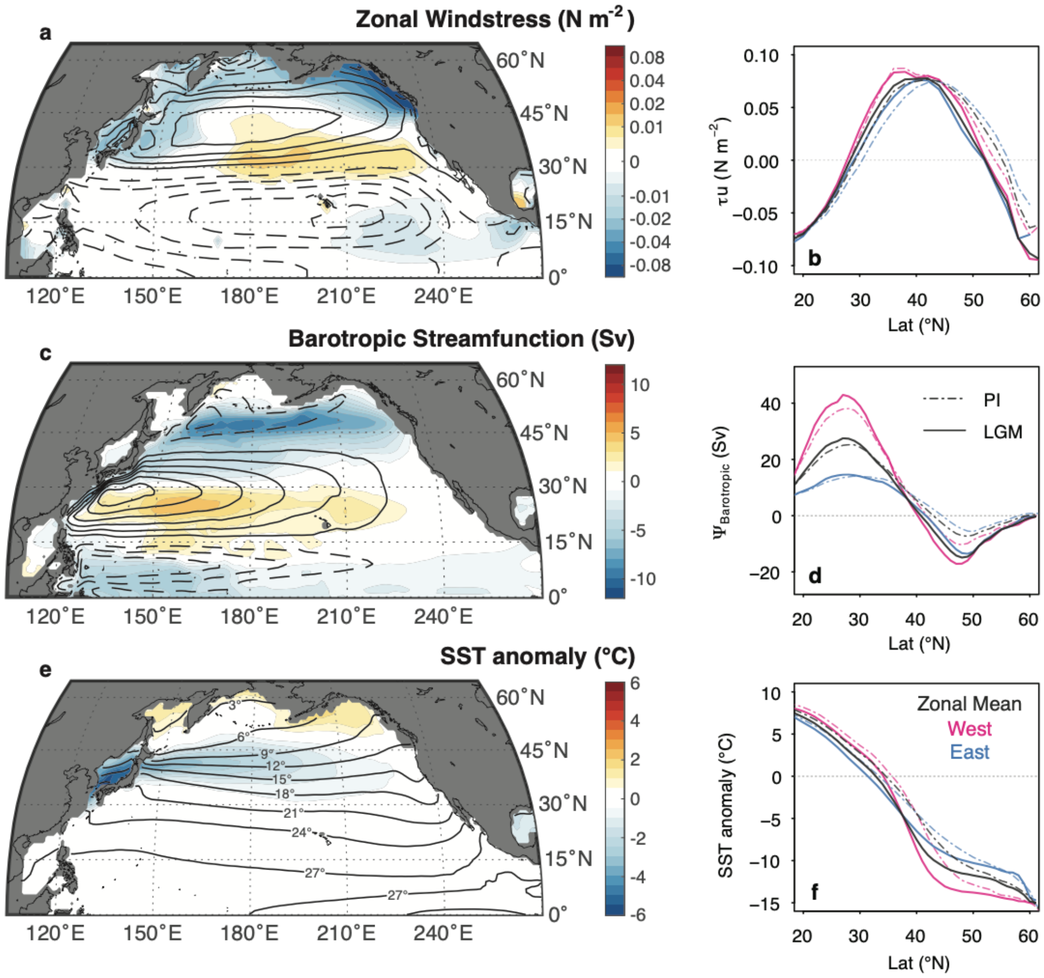

Figure 3 PMIP3 ensemble mean of **(a)** LGM-PI zonal windstress (τu), with the PI climatology indicated by contours (contour interval of 0.04 N m^{-2}; dashed is negative and solid is positive), **(b)** zonal average and averages east and west of 180° of zonal windstress in LGM and PI, **(c)** LGM-PI barotropic streamfunction ($\Psi_{barotropic}$), with the PI climatology indicated by contours (contour interval of 10 Sv; dashed is negative and solid is positive), **(d)** zonal average and averages east and west of 180° of the barotropic streamfunction in LGM and PI, **(e)** LGM-PI SST anomaly from global mean, with the PI climatology indicated by the contours **(f)** zonal average and averages east and west of 180° of the SST anomaly from global mean in the LGM and PI.

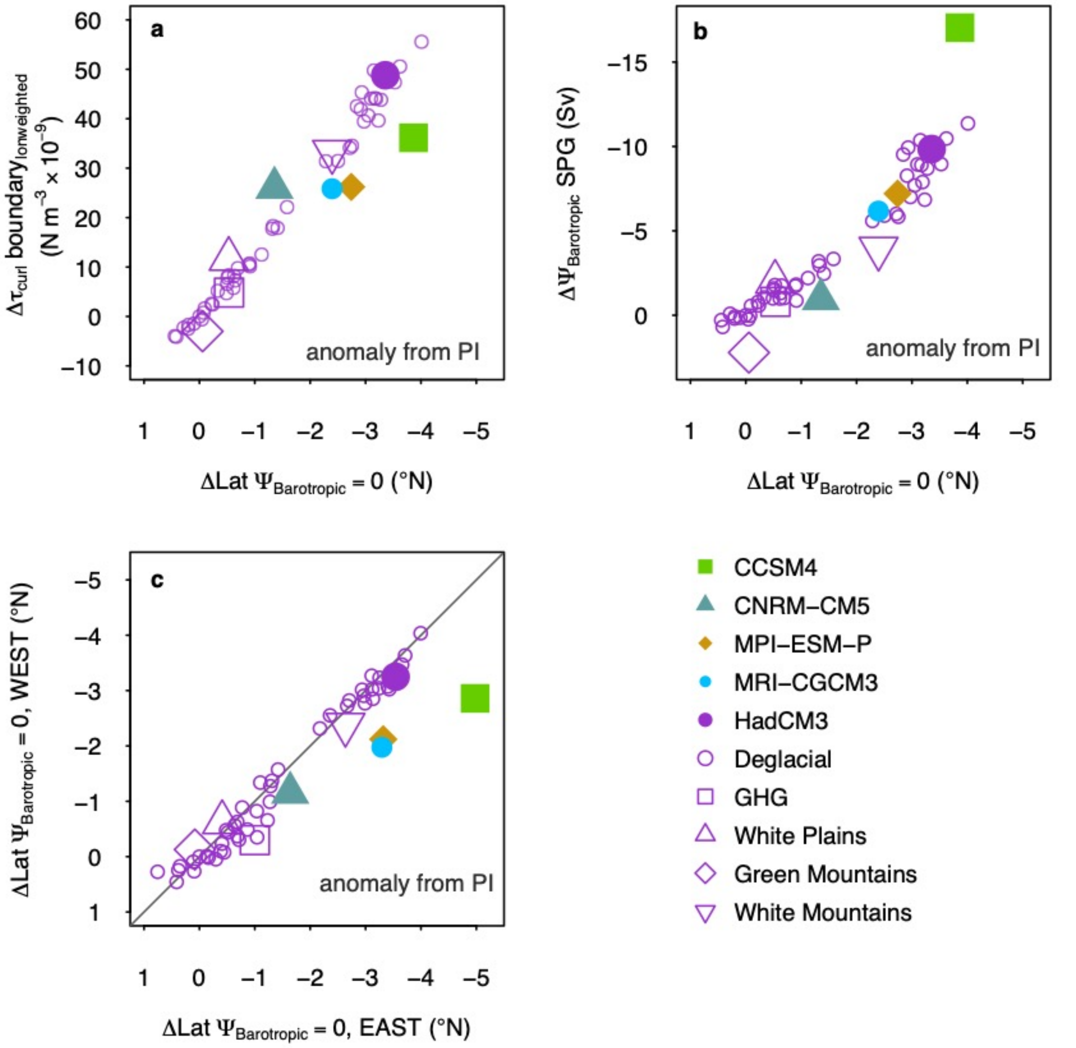

Figure 4 **(a)** LGM-PI change in latitude of zonal-mean $\Psi_{barotropic} = 0$ versus change in longitudinally weighted mean $\nabla \times \tau$ across the southern boundary of the subpolar gyre (38-50 °N) ($\Delta\tau_{curl}$boundary$_{lonweighted}$) **(b)** LGM-PI change in latitude of zonal mean $\Psi_{barotropic} = 0$ versus change in $\Psi_{barotropic}$ within the subpolar gyre (maximum north of 40°) **(c)** LGM-PI change in latitude of zonal mean $\Psi_{barotropic} = 0$ east and west of 180°. Green Mountains = LGM ice sheet topography with PI albedo, White Plains = LGM ice sheet albedo with PI topography, White Mountains = LGM ice sheet topography and albedo.

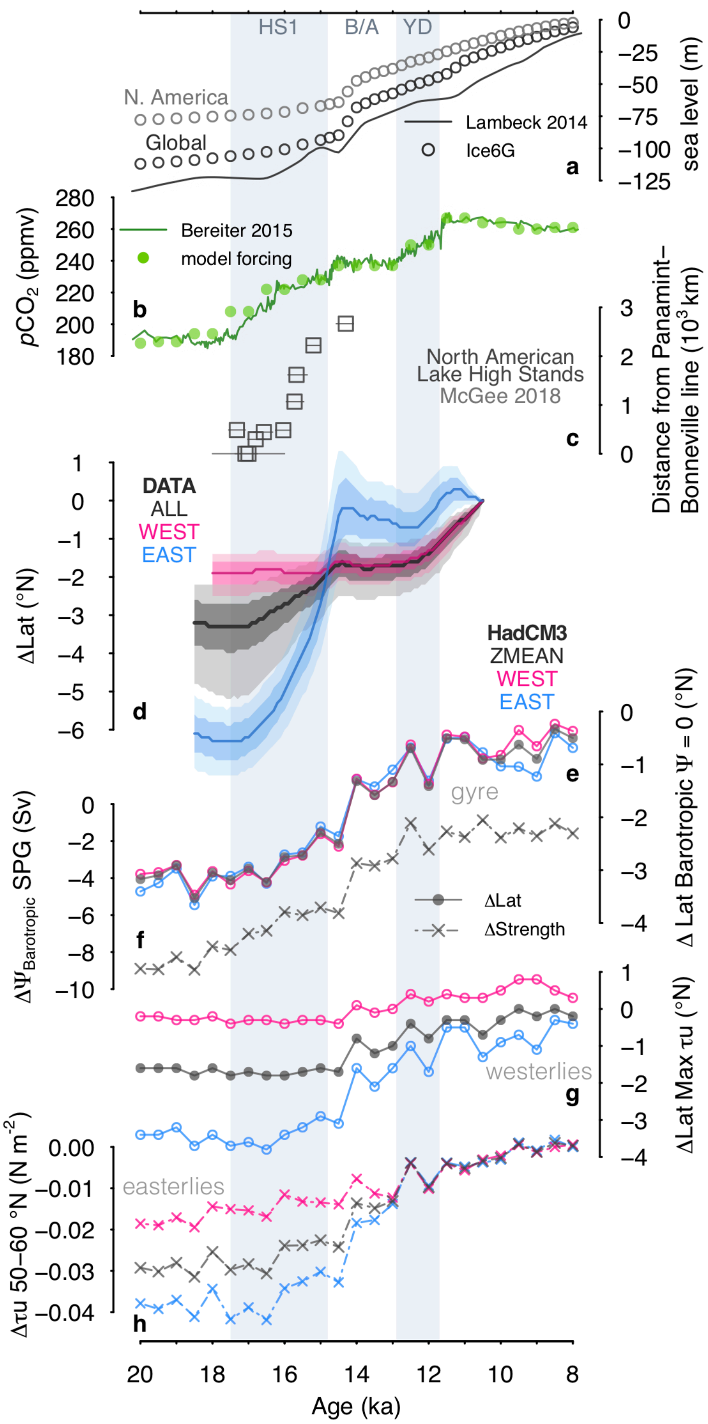

Figure 5 **(a)** Sealevel curve of Lambeck *et al.* (2014) and sealevel equivalent of global and North American ice sheet volume in the ICE6Gc ice sheet reconstruction **(b)** Atmospheric $p\mathrm{CO}_2$ record of Bereiter *et al*. (2015) and $p\mathrm{CO}_2$ forcing used in model **(c)** north-westward progression of lake high stands in southwestern North America (McGee *et al*., 2018) **(d)** reconstructed change in gyre boundary position with 68% and 95% confidence intervals (east and west is east and west of 180°) **(e)** modelled change in gyre boundary position **(f)** modelled change in subpolar gyre strength (maximum north of 40°) **(g)**

modelled change in westerly position (determined as latitude of maximum zonal windstress, τu) **(h)** modelled change in wind stress strength exerted by the easterlies (determined as mean τu between 50-60 °N). For model results solid lines denote a change in position, and the dashed lines denote a change in strength. See Figure S8 for meridional profiles of SST, barotropic stream function, and zonal wind stress.

supporting information to

Wind-driven evolution of the North Pacific subpolar gyre over the last deglaciation

William R Gray[1,2]*, Robert CJ Wills[3], James WB Rae[2], Andrea Burke[2], Ruza F Ivanovic[4], William HG Roberts[5], David Ferreira[6], Paul J Valdes[7]

[1]Laboratoire des Sciences du Climat et de l'Environnement (LSCE/IPSL), Gif-sur-Yvette, France
[2]School of Earth and Environmental Science, University of St Andrews, UK
[3]Department of Atmospheric Sciences, University of Washington, USA
[4]School of Earth & Environment, University of Leeds, UK
[5]Geography and Environmental Sciences, Northumbria University, UK
[6]Department of Meteorology, University of Reading, UK
[7]School of Geographical Sciences, University of Bristol, UK

*corresponding author: william.gray@lsce.ipsl.fr

The R code to perform the analysis is available at https://github.com/willyrgray/npac_gyres
The compiled $\delta^{18}O$ data is available at https://doi.pangaea.de/10.1594/PANGAEA.912229

Table of contents

Other supporting information not included in this file *- Dataset S1, Table S2*

Using planktic foraminiferal $\delta^{18}O$ to trace the gyre boundary

The $\delta^{18}O$ of the planktic foraminiferal calcite ($\delta^{18}O_{\text{calcite}}$) is a function of the $\delta^{18}O$ of seawater ($\delta^{18}O_{\text{water}}$, which is closely related to salinity), and the temperature dependant fractionation between calcite and water ($\delta^{18}O_{\text{calcite-water}}$); specifically, the fractionation between calcite and water is described by a fractionation factor ($\alpha_{\text{calcite-}}$

$_{\text{water}}$ = [^{18}O/^{16}O]$_{\text{calcite}}$ / [^{18}O/^{16}O]$_{\text{water}}$) which is related to temperature via,

$$1000 \ln \alpha_{\text{calcite-water}} = 18.03(10^3 T^{-1}) - 32.42$$

where T is temperature in Kelvin (Kim and O'Neil, 1997).

Our ability to use the planktic foraminiferal $\delta^{18}O_{\text{calcite}}$ to trace the gyre boundary comes from the dominance of the temperature signal over that of $\delta^{18}O_{\text{water}}$ in driving the meridional pattern of $\delta^{18}O_{\text{calcite}}$ across the basin; the temperature signal is 4-5 times greater than the $\delta^{18}O_{\text{water}}$ signal (Figure 1). As the spatial temperature pattern across the basin is primarily governed by the gyre circulation, with the steepest meridional temperature gradient (and thus meridional $\delta^{18}O_{\text{calcite}}$ gradient) at the gyre boundary, we can use the meridional profiles of temperature (and thus $\delta^{18}O_{\text{calcite}}$) to track the movement of the gyre boundary. Coupled climate models demonstrate a very tight coupling between the LGM-PI change in latitude of gyre boundary (defined where barotropic stream function = 0) and LGM-PI change in the latitude of maximum latitudinal gradient in sea surface temperature (SST) (Figure S1). As no mechanism exists to drive changes in $\delta^{18}O_{\text{water}}$ of the same magnitude as the changes in $\delta^{18}O_{\text{calcite-water}}$ fractionation from the large temperature difference between the gyres (Figure 1d), the temperature signal will always dominate over the $\delta^{18}O_{\text{water}}$ signal in determining the spatial pattern of $\delta^{18}O_{\text{calcite}}$ (Figure 1e) across the basin and the maximum meridional $\delta^{18}O_{\text{calcite}}$ gradient (Figure 1f); thus, while there are likely to be local changes in $\delta^{18}O_{\text{water}}$ across the basin, the steepest part of the meridional $\delta^{18}O_{\text{calcite}}$ gradient will always be determined by temperature, allowing us to use meridional profiles of $\delta^{18}O_{\text{calcite}}$ to track the position of the gyre boundary through time.

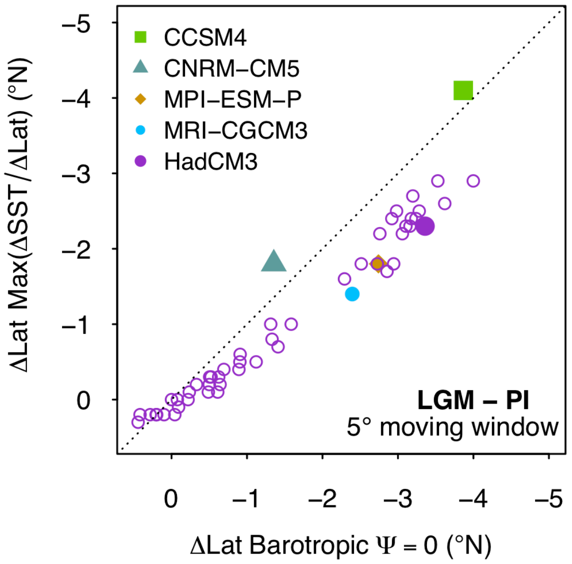

Figure S1 Modelled zonal mean LGM-pre-industrial (PI) change in latitude of gyre boundary (defined where barotropic stream function = 0) versus LGM-PI change in latitude of maximum meridional gradient in sea surface temperature (SST) within a 5° moving window; the close relationship demonstrates past changes in the position of the maximum gradient in SST/Lat (and thus ~$\delta^{18}O_{calcite}$/Lat) can be used to trace changes in the position of the gyre boundary.

We model the compiled $\delta^{18}O_{calcite}$ data (see below) as a function of latitude, using a Gaussian generalized additive model (GAM) (Wood, 2011; Wood *et al.*, 2016) in the *mgcv* package in R (R core Team) at 100 yr timesteps from 18.5 to 10.5 ka (the time interval/resolution for which we have sufficient spatial and temporal coverage in our dataset; Figure 1),

$$\delta^{18}O_{calcite} = \beta_0 + f(Lat) + \varepsilon$$

where β_0 is the intercept term, ε is random error, and f(Lat) is a smooth function, which can be represented as the sum of the underlying basis functions,

$$f(Lat) = \sum_{j=1}^{k} b_j(Lat)\beta_j$$

where b_j is the evaluation of the j^{th} basis function at the value of Lat, and β_j is the estimated coefficient or weight of that basis function. We sum over the weighted values of k basis functions (j = 1, 2, …, k), which comprise of reduced rank thin plate regression splines (Wood, 2011; Wood et al., 2016; Simpson, 2018). Here, *k* was set to 8, although the value of *k* has little effect on the smooth function. The smooth function is estimated by minimising the penalised sum of squares; the penalty term imposes smoothness by calculating the integrated square of the second derivative of the spline (Wood, 2011; Wood et al., 2016; Simpson, 2018),

$$penalty = \lambda \int f''(Lat)^2 dLat$$

with the smoothness parameter (λ) controlling the extent to which the penalty term contributes to the likelihood of the model, with larger λ giving a smoother function (Wood, 2011; Wood et al., 2016; Simpson, 2018). The smoothness parameter was determined using Restricted Maximum Likelihood (REML, Reis and Ogden, 2009; Wood *et al.*, 2016). Uncertainty envelopes on the fitted models (Figure 2) represent the 68% and 95% Bayesian credible intervals. The reader is directed to Simpson (2018) for a detailed overview of GAM methodology.

Figure S2 (below) GAM fits to $\delta^{18}O_{calcite}$ data as a function of latitude at 500 year timesteps from 18.5 to 10.5 ka (colours indicate age); the GAM fit to Holocene $\delta^{18}O_{calcite}$ data (10.5 ka) is shown in dark grey. The portion of the curve within the latitudinal band used to calculate the shift in gyre position (see Fig. S5) is shown by the solid line; at each timestep we calculate the latitudinal shift that minimises the Euclidean distance (along the y-axis) between the solid part of the coloured curve and the solid part of the grey curve. Data are the combined east-west dataset (marked ALL on Figure 4). Note, the reconstruction in Figure 5 uses time-steps of 100 years; here, in the interests of space, we only show the meridional profiles at time-steps of 500 years.

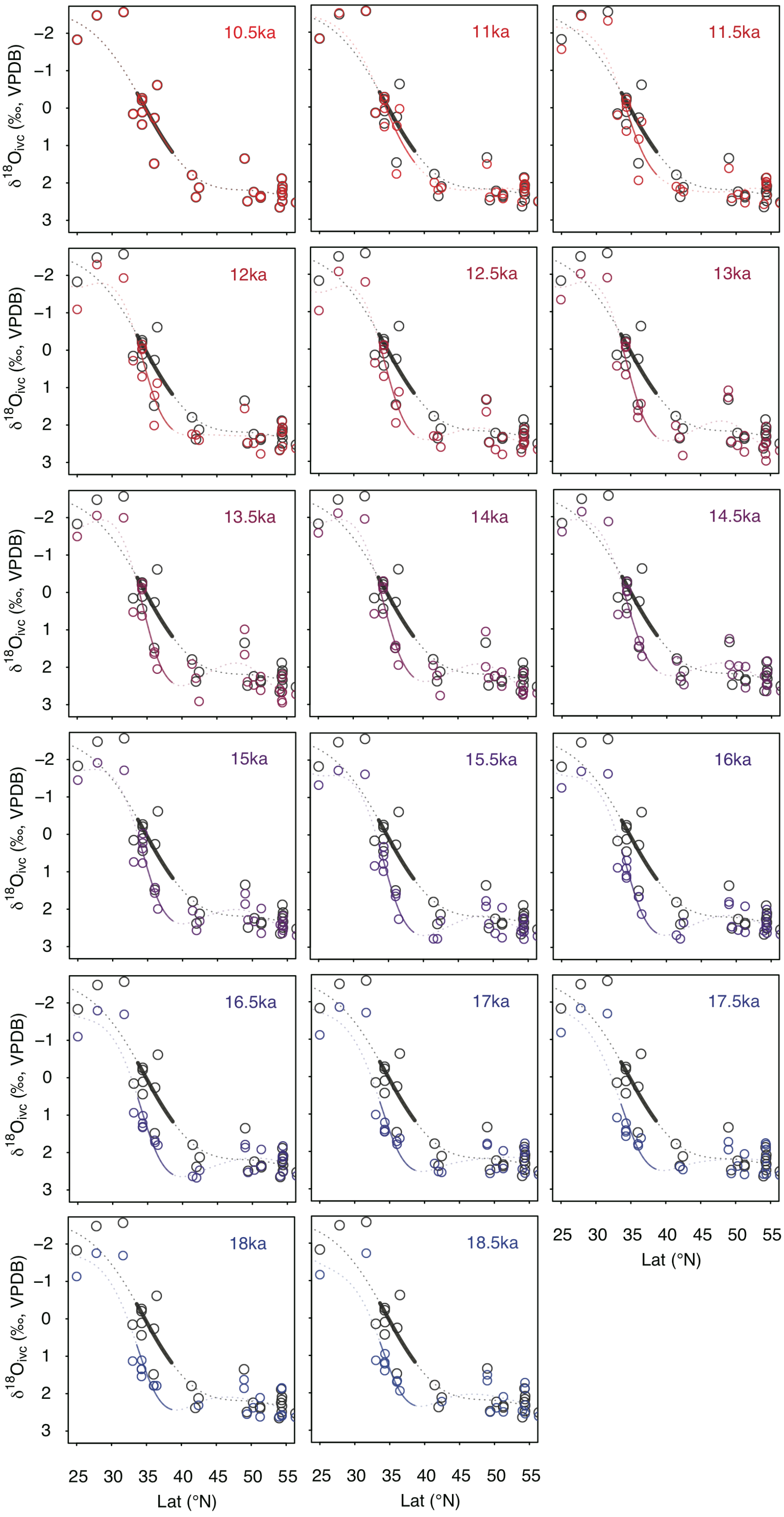
10.5ka
11ka
11.5ka
12ka
12.5ka
13ka
13.5ka
14ka
14.5ka
15ka
15.5ka
16ka
16.5ka
17ka
17.5ka
18ka
18.5ka
δ18Oivc (‰, VPDB)
−2
−1
0
1
2
3
25
30
35
40
45
50
55
Lat (°N)

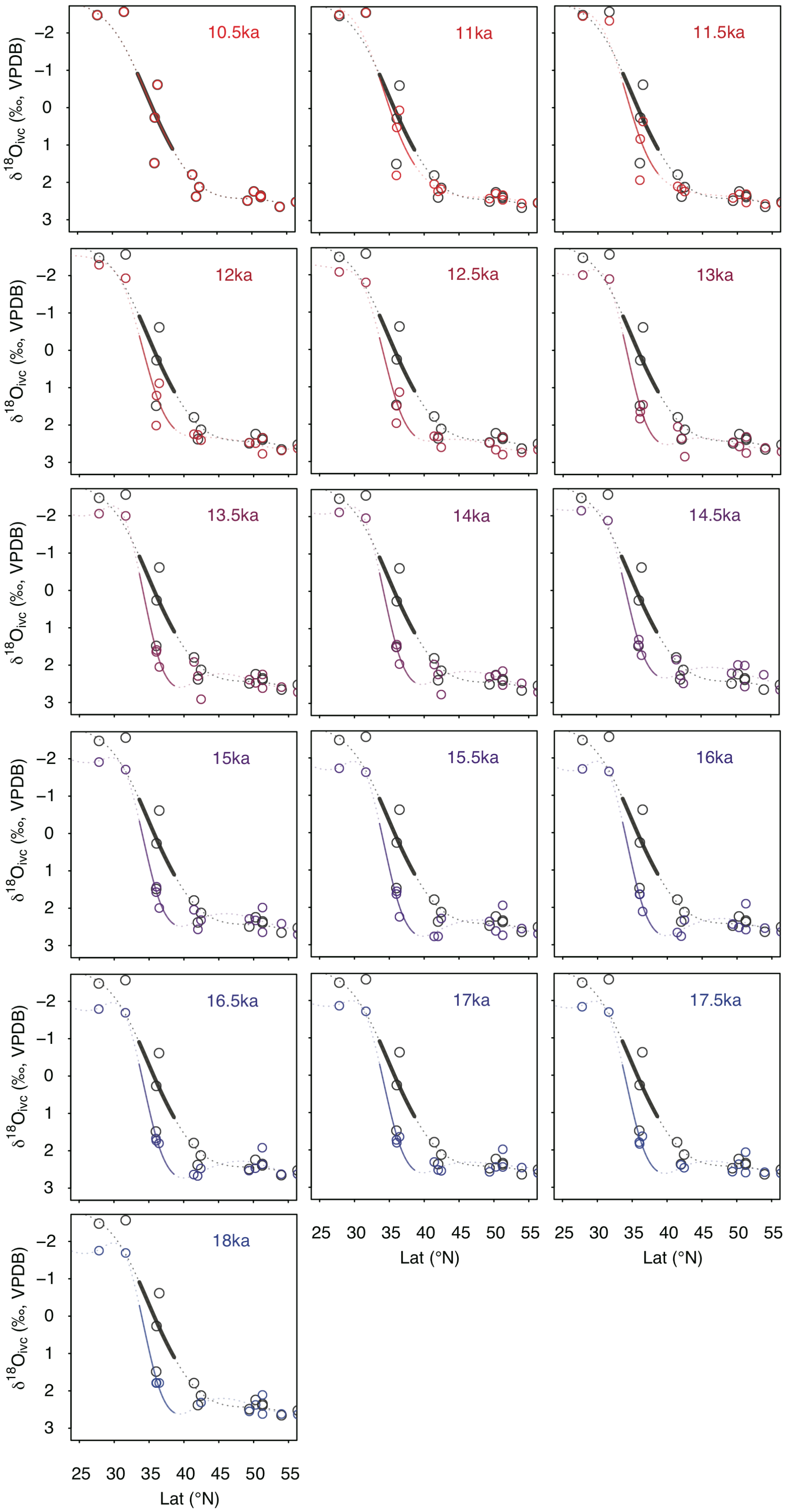

Figure S3 As figure S2, however data are from west of 180°.

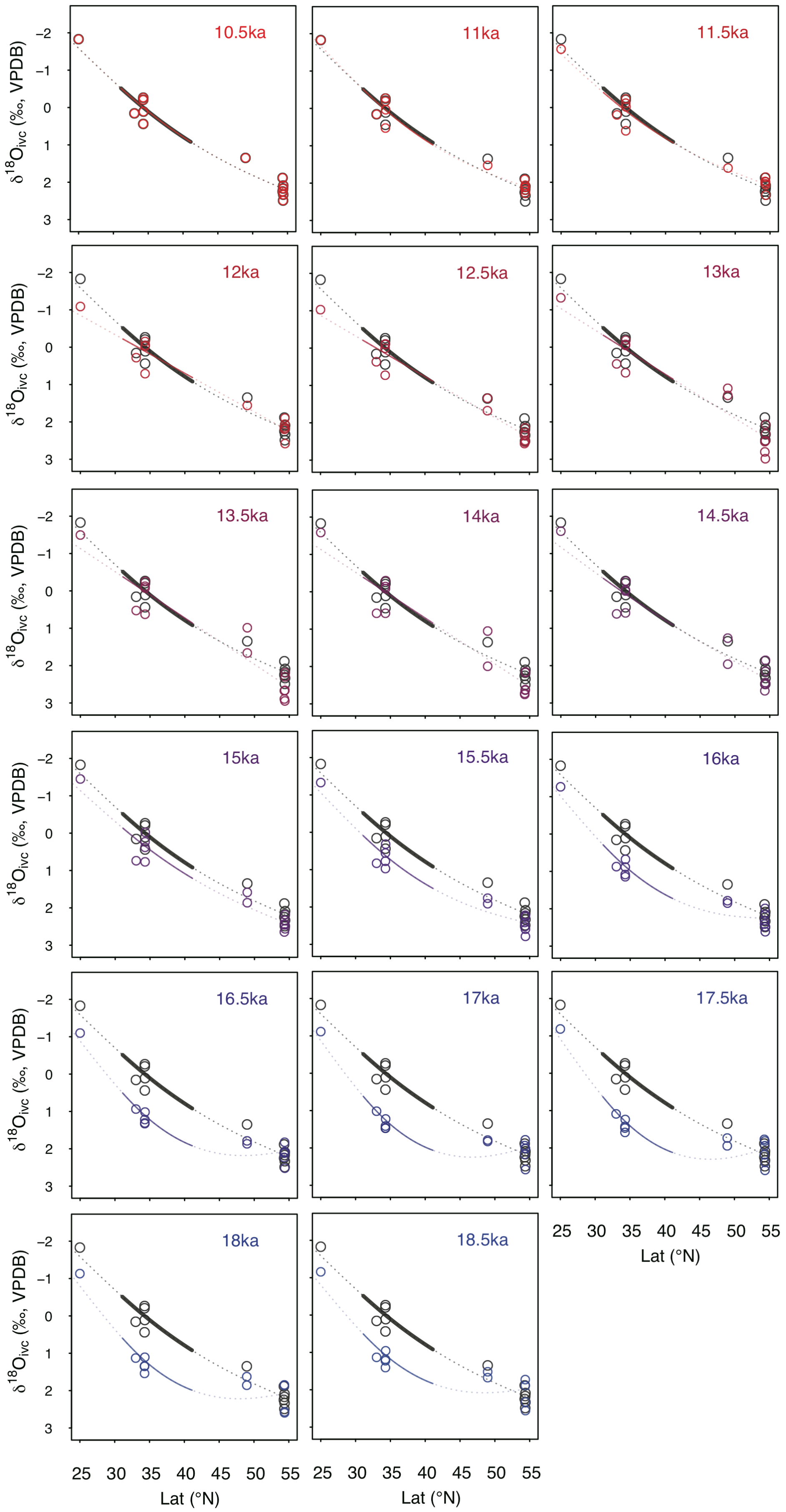

Figure S4 As figure S2, however data are from east of 180°.

We calculate the change in gyre boundary position over deglaciation as the latitudinal shift (x°) that minimises the Euclidean distance (L^2) between the Holocene (taken as 10.5±0.5 ka) $\delta^{18}O_{calcite}$~latitude GAM fit and the GAM fit to each time step, within a latitudinal band spanning the gyre boundary; this latitudinal band is centred around the maximum gradient in $\delta^{18}O_{calcite}$ versus latitude in the Holocene data within a 5° moving window (36.1 °N). In the combined dataset from the east and west, and the data from the west only, we calculate the latitudinal shift using a 5° latitudinal band (i.e. 33.6 to 38.6 °N), and we note the size of this latitudinal band has only a negligible effect on our results (Fig. S5); as the gyre boundary (and thus meridional temperature and $\delta^{18}O_{calcite}$ gradient) is more diffuse in the east, we use a slightly larger window of 10° (i.e. 31.1 to 41.1 °N).

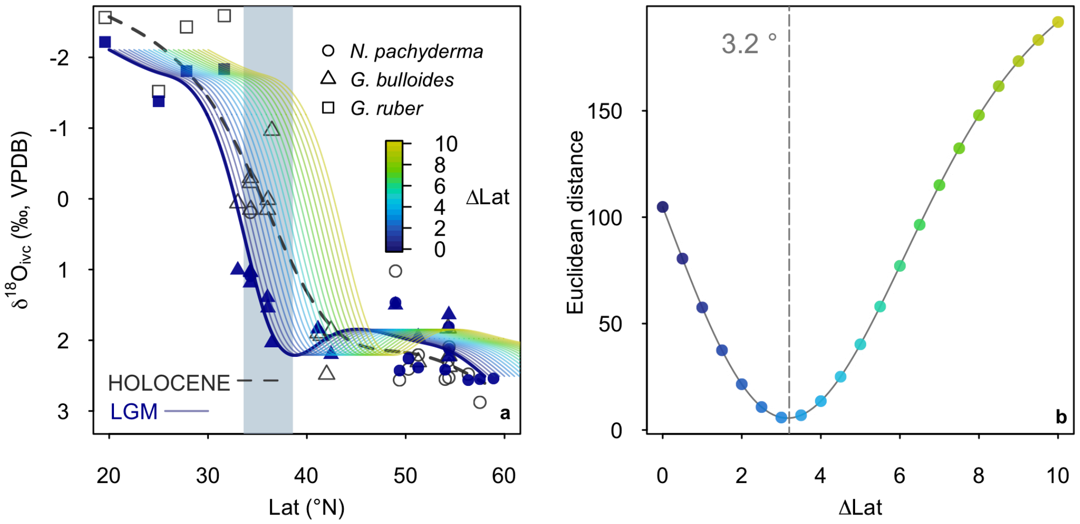

Figure S5 method used to calculate the shift in gyre boundary position **(a)** at each time step (here LGM, 18.5 ka) we calculate the gyre boundary shift as the latitudinal shift (x°, in 0.1 ° increments from 0 to 10 degrees) that minimises the Euclidean distance **(b)** within a specified latitudinal band (grey box in (a) between the GAM fit to the timestep (solid line) and the Holocene (dashed line) in data is calculated. The coloured lines in (a) show the LGM GAM fit shifted north in 0.5° increments, and the coloured dots in (b) show the Euclidean distance from the Holocene line at each increment, with the colour indicating the degree to which the curve has been shifted.

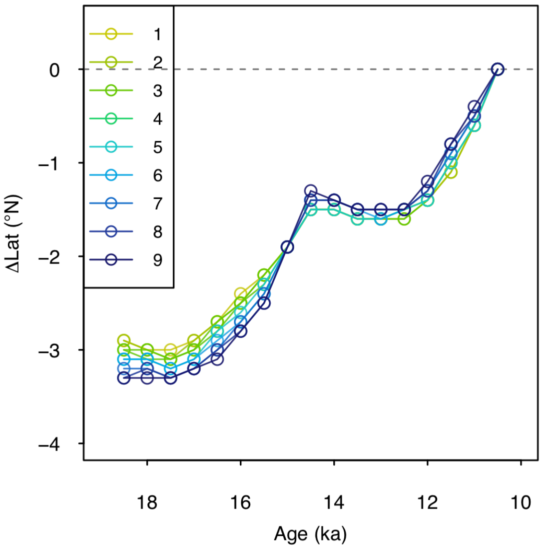

Figure S6 (a) calculated change in the position of the gyre boundary using different sizes of latitudinal band (between 1° and 9°) in which the Euclidean distance between the GAM fits is calculated; the size of latitudinal band (the grey box in figure S5a above) has very little effect on the results.

We note that the steepest part of the Holocene curve (~36.1 °N) using the combined dataset from the east and west, is further south than the zonal mean position of the gyre boundary today (~40 °N). This is due to the westward bias within the dataset (i.e. there are many more sites in the west relative to the east within the dataset), and the gyre boundary is located slightly further south in the west relative to the zonal mean; the maximum meridional gradient in mean annual SST is found at ~36 °N along the western margin of the basin (Boyer et al., 2013), in good agreement with our reconstruction.

We also note that if we use a totally different method to calculate the change in position of the gyre boundary, simply calculating the change in latitude in the steepest part of the meridional $\delta^{18}O_{calcite}$ gradient (within a 5° moving window), we arrive at a very similar estimate of a ~2.6° southward shift between the Holocene and LGM. This method is more prone to anomalous values at the latitudinal extremes; hence we opt for the method of calculating the latitudinal shift that minimises the Euclidean distance between timesteps within a defined latitudinal band described above. The agreement between the two methods is, however, reassuring.

Planktic foraminiferal $\delta^{18}O_{calcite}$ *compilation*

We compiled all available planktic foraminiferal calcite δ^{18}O from cores across the North Pacific. Compiled records include δ^{18}O measured on *G. ruber*, *G. bulloides*, and *N. pachyderma*. All data were kept on the original age models, except in the case when data were only available on uncalibrated ^{14}C age models, in which case the ^{14}C data were recalibrated using INTCAL13 (Reimer et al., 2013) using an average of the modern reservoir age at each site and a regional glacial increase of +400 years with large uncertainties (±500 years). All $\delta^{18}O_{calcite}$ data along with the core, location, water depth, species, sediment depth, age, and original data reference are given in Table S1. We only include cores spanning the interval between 10.5 to 18.5 ka with an average resolution of >1 point per ka; the average resolution of the individual cores during deglaciation is ~1 point/125 years. We exclude core EW0408-26/66JC from the compilation (Praetorious and Mix, 2014); this core is located in close proximity to the terminus of a glacier, and comparing the $\delta^{18}O_{calcite}$ data of this core to other cores within the subpolar gyre demonstrates planktic foraminiferal $\delta^{18}O_{calcite}$ data from this core primarily reflect local meltwater changes, rather that wider oceanographic conditions in the subpolar gyre (Figure S7). The compiled dataset is given in Dataset S1 and is available at https://doi.pangaea.de/10.1594/PANGAEA.912229.

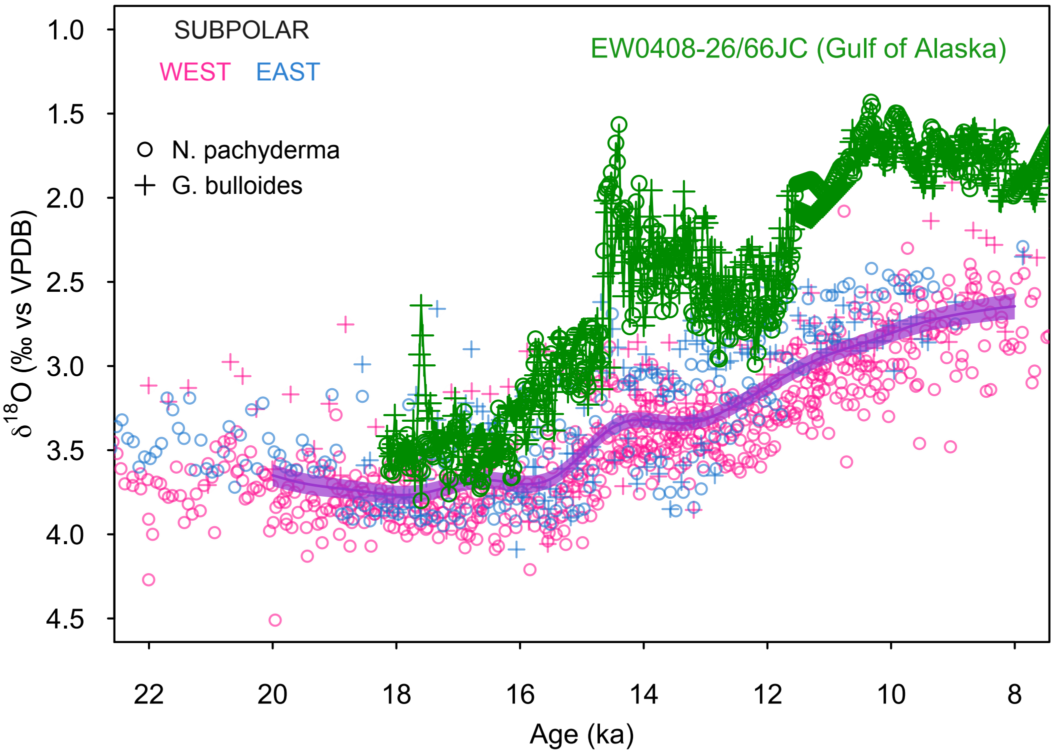

Figure S7 Foraminiferal $\delta^{18}O_{calcite}$ from the subpolar gyre over deglaciation. A GAM fit with to all the data (excluding core EW0408-26/66JC) is shown by the purple line, with 68% Bayesian credible interval shaded. Data from core EW0408-26/66JC (Praetorius and Mix, 2014) is shown in green.

Seasonality of planktic foraminifera

Our approach assumes that any change in seasonal bias relating to the habitat preference of foraminifera are small relative to the change in temperature due to the movement of the gyre boundary. The validity of this approach is supported by sites where $\delta^{18}O_{calcite}$ has been measured on more than one species of foraminifera, such as core ODP Site 893 or MD02-2489 (Figure 1 and Figure 2). At these sites, foraminiferal species with habitat temperature preferences that are known to be different (*G. bulloides* and *N. pachyderma*, e.g. Taylor *et al.*, 2018) show very similar changes down core, with a Holocene-LGM change that is identical (within error); this suggests any changes relating to changes seasonal bias are likely to be insignificant in our reconstruction.

Sea surface temperature and %Opal data

We compiled Mg/Ca and $U^{K'}_{37}$ sea surface temperature (SST) data from across the North Pacific (Mg/Ca: Reitdorf et al., 2013; Gebhardt et al., 2008; Rodriguez Sanz et al., 2013; Taylor et al., 2015; Sagawa et al., 2006; Sagawa et al., 2008; Pak et al., 2012; Kubota et al., 2010; Gray et al, 2018. $U^{K'}_{37}$: Minoshima et al., 2007; Seki, 2004; Harada et al., 2004; Harada, 2006; Harada et al., 2008; Inagaki et al., 2009; Herbert et al., 2001; Sawada et al., 1998; Yamamoto et al., 2004; Isono et al., 2009). All age models are as given in the original publication. All Mg/Ca and $U^{K'}_{37}$ data were recalibrated (see below) and the temperature change during the LGM (Figure 2c) is given as a difference to both proxy temperature in the Holocene, and to mean annual climatological temperature from the WOA13 (Boyer et al., 2013).

While the direct temperature sensitivity of Mg/Ca in planktic foraminifera is ~6% per °C (Gray et al., 2018b; Gray and Evans, 2019), due to the effect of temperature on pH through the disassociation constant of water (K_w), the 'apparent' Mg/Ca temperature sensitivity is higher (Gray et al., 2018b). Thus, we calculate the change in temperature from the change in Mg/Ca at each site using a temperature sensitivity of 8.8%, derived from laboratory cultures (Kisakürek et al., 2008), which encompasses both the direct temperature effect and the temperature-pH effect, with a Mg/Ca-pH sensitivity of ~ -8% per 0.1 pH unit (Lea et al., 1999; Russell et al., 2004; Evans et al., 2016; Gray et al., 2018b; Gray and Evans, 2019). Mg/Ca is also influenced by salinity, with a sensitivity of ~3-4% per PSU (Hönisch et al, 2013; Gray et al., 2018b; Gray and Evans, 2019). As we are primarily interested in (qualitative) changes in meridional SST pattern, we make no attempt to account for the whole ocean effects of salinity or pH downcore. The combined effect of the whole-ocean increase in salinity (due to sea level), and the increase in surface ocean pH (due to lower atmospheric CO_2) means changes in temperature derived from changes in Mg/Ca are likely to be cold-biased by ~1.5 °C during the LGM (Gray and Evans, 2019). For $U^{K'}_{37}$, the change in temperature at each site was calculated using the calibration of Prahl et al., 1988; the temperature range in this study is too low to be substantially effected by the non-linearity of $U^{K'}_{37}$ (e.g. Tierney and Tingley, 2018).

We analyse the North Pacific %Opal compilation of Kohfeld and Chase (2011) to look for qualitative changes in the meridional pattern of productivity over the last deglaciation. Due to the high nutrient supply from upwelling, productivity in the SPG is an order of magnitude higher than the STG. A southward expansion of the gyre boundary should thus result in an increase in productivity within the transition zone; transition zone sites show a ~25% increase in %Opal on both sides of the basin during the LGM (Figure 2d) consistent with nutrient-rich subpolar waters moving further south during the LGM and increasing local productivity.

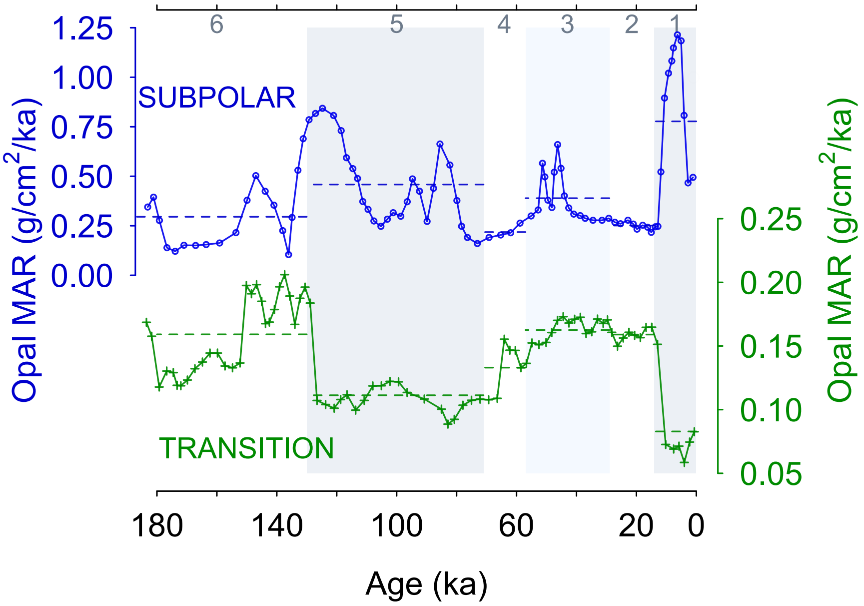

Figure S8 Opal Mass Accumulation Rate data from core KH99-03 in the SPG (Narita et al., 2002) and core NCG108 in the transition zone (Maeda et al., 2002). Dashed lines show mean value for each marine isotope stage (MIS). Grey shading shows MIS 1, 3 and 5. Transition zone and subpolar waters show an anti-phased relationship in Opal MAR over the last glacial cycle.

General Circulation Models

We assess differences in North Pacific barotropic stream function, wind stress curl, zonal wind stress, and SST between LGM and pre-industrial conditions as represented by four coupled climate models (CCSM4, CNRM-CM5, MPI-ESM-P and MRI-CGCM3). All models are part of the Coupled Model Intercomparison Project phase 5 (CMIP5, Taylor et al., 2012). We only used the four models where both wind stress and barotropic stream function data are available. Orbital parameters, atmospheric greenhouse gas concentrations, coastlines and ice topography for the LGM simulations are standardized as part of the Paleoclimate Model Intercomparison Project phase 3 (PMIP3) (Braconnot *et al.* 2012, Taylor *et al.* 2012). Ensemble means are computed by first linearly interpolating to a common grid, and are 4-model means of 100-year climatologies; uncertainties in these centennial averages due to internal variability are negligible.

Using a single model (HadCM3) we look at runs where the model greenhouse gas, ice sheet albedo, ice sheet topography are changed individually ('Green Mountains, White Plains') as described in Roberts and Valdes (2017). The 'Green Mountains, White Plains' runs use the ICE5G ice sheet reconstruction (Peltier *et al.*, 2004), whereas the deglacial 'snapshot' runs (below) use the ICE6G ice sheet reconstruction (Peltier *et al.*, 2015). The change in gyre boundary position with each forcing are as follows: GHG = -0.5 °N; Albedo = -0.5 °N; Topography = -0.05 °N; Albedo + Topography = -2.4°N; ALL (although with the smaller ICE6G ice sheet) = -3.4 °N.

We also explore changes through time over the deglaciation using a series of HadCM3 equilibrium-type simulations where all forcings and model boundary conditions are changed at 500-year intervals broadly adhering to the PMIP4 last deglaciation protocol (Ivanovic et al., 2016). These simulations use the ICE6GC ice sheet reconstruction and 'melt-uniform' scenario for ice sheet meltwater; i.e. freshwater from the melting ice sheets is NOT routed to the ocean via coastal outlets. Instead, water is conserved by forcing the global mean ocean salinity to be consistent with the change in global ice sheet volume with respect to present. Note, these deglacial simulations are not transient, but are equilibrium-type experiments that begin from the end of the 1750-year long simulations run by Singarayer et al. (2011). At each 500-year interval (21.0 ka, 20.5 ka, 20.0 ka…0.5 ka, 0.0 ka), all boundary conditions and forcings are updated according to the more recent literature (presented by Ivanovic et al., 2016) and held constant for the full 500-year duration of the run. The climate means and standard deviations used here are calculated from the last 50 years of each simulation (i.e. year 451-500, inclusive). More information on these runs can be found in the supplement to Morris et al. (2018), noting that we use the raw model output and not the downscaled and bias-corrected data used in the previous publication. Zonal mean changes in SST anomaly (from global mean), barotropic stream function, and zonal wind stress at each time step are shown below (Fig. S9).

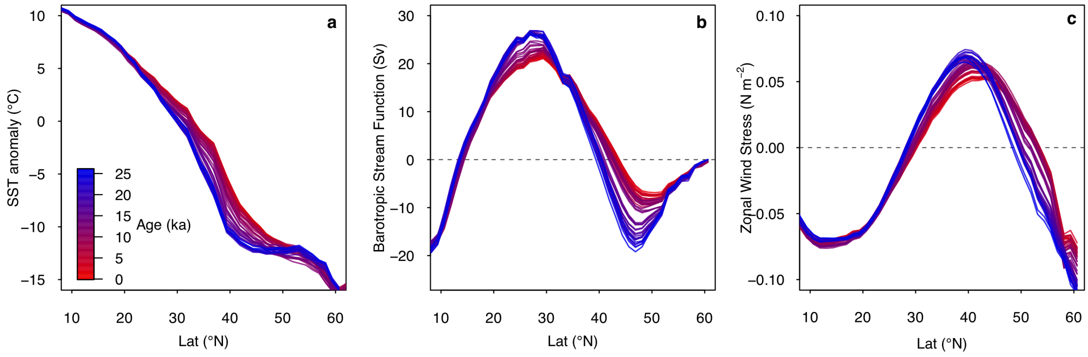

Figure S9 Deglacial evolution of zonal mean **(a)** SST anomaly (relative to global mean) **(b)** barotropic stream function **(c)** zonal wind stress in the HadCM3 simulations.

Eastern boundary test

To test if there is an influence of coastal upwelling on the data in the east (i.e. a signal of some other control on latitudinal temperature anomaly [and thus latitudinal $\delta^{18}O_{calcite}$ anomaly] besides change in gyre position) we compare the ensemble mean SST along the eastern boundary of the basin (taken as the first oceanic grid point west of land during the LGM) to the zonal mean, and zonal mean east of the dateline (Fig. S10). The models show no indication of a strong influence of coastal upwelling, which would manifest as an anomalous cooling relative to the zonal mean. This analysis suggests coastal upwelling is unlikely to be having a significant effect on our results, although the simulated coastal upwelling may be poorly represented due to the resolution of the models.

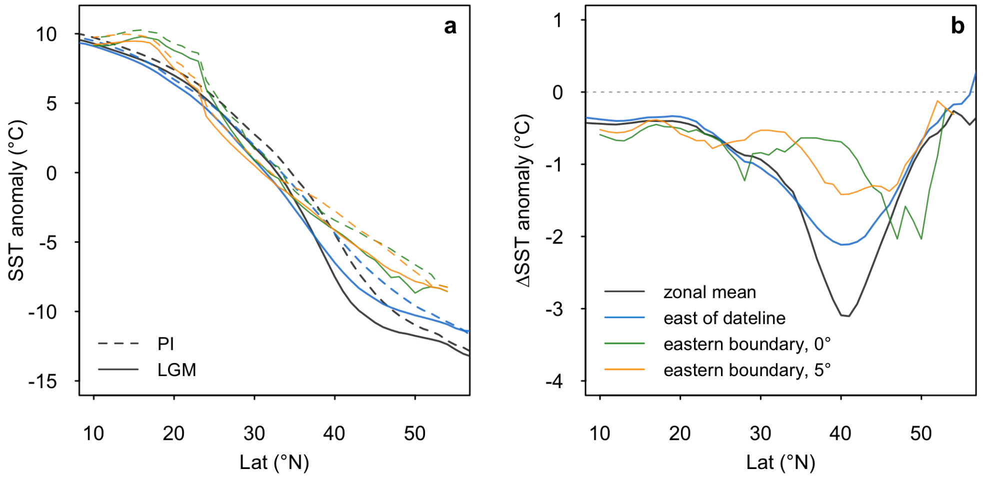

Figure S10 (a) LGM and PI SST anomaly (from global mean), and **(b)** LGM-PI SST anomaly in different longitudinal bins; zonal mean (grey), zonal mean east of the dateline (180°, blue), along the eastern boundary of the basin (green), and 5° seaward from the eastern boundary of the basin (orange). Note, the gyre boundary s located slightly further north along the eastern margin relative to the zonal mean and zonal mean east of the dateline.

HS1 Freshwater test

The release of large amounts of freshwater into the eastern subpolar North Pacific has been suggested over deglaciation, at ~17.5 ka (Maier *et al* 2018). The release of freshwater into the eastern subpolar North Pacific is evident in an increase in the

$\delta^{18}O_{calcite}$ difference between the mixed-layer dwelling species *G. bulloides* and the slightly deeper-dwelling species *N. pachyderma* in core MD02-2489 (54.39°N, -148.92°E) at this time; during this interval *G. bulloides* becomes ~0.6 ‰ more depleted than *N. pachyderma*. To test if this release of freshwater may be influencing our gyre boundary reconstruction we re-run the gyre-boundary analysis, however removing the *G. bulloides* data from core MD02-2489; the results are identical to the gyre boundary reconstruction including the *G. bulloides* data demonstrating that the effect of freshwater release has very little effect on our gyre boundary reconstruction. This is because the change in $\delta^{18}O_{calcite}$ from the freshwater release (~0.6 ‰, equivalent to ~2 PSU freshening) is very small compared to the large change in $\delta^{18}O_{calcite}$ resulting from the temperature difference between the gyres (~5.5 ‰). Localised freshwater inputs, while having a large effect locally, do very little to change the pattern of $\delta^{18}O_{calcite}$ at the basin scale.

Table S1 Compiled planktic foraminiferal $\delta^{18}O_{calcite}$ records. The compiled will be made available on Pangea.

Core	Lat (°N)	Lon (°E)	Species	Reference
MD02-2489	54.39	-148.92	*N. pachyderma*	Gebhardt et al 2008
MD02-2489	54.39	-148.92	*G. bulloides*	Gebhardt et al 2008
PAR87A-10	54.36	-148.46	*G. bulloides*	Zahn et al 1991
PAR87A-10	54.36	-148.46	*N. pachyderma*	Zahn et al 1991
PAR87A-02	54.29	-149.61	*G. bulloides*	Zahn et al 1991
PAR87A-02	54.29	-149.61	*N. pachyderma*	Zahn et al 1991
MD02-2496	48.97	-127.03	*N. pachyderma*	Taylor et al 2015
MD02-2496	48.97	-127.03	*G. bulloides*	Taylor et al 2015
ODP1017	34.32	-121.60	*G. bulloides*	Pak et al 2012
ODP893	34.23	-120.04	*N. pachyderma*	Hendy et al 2002
ODP893	34.23	-120.04	*G. bulloides*	Hendy et al 2002
MD02-2503	34.28	-120.04	*G. bulloides*	Hill et al 2006
AHF-28181	33.01	-119.06	*G. bulloides*	Mortyn et al 1996
MD05-2505	25.00	-112.00	*G. ruber*	Rodríguez-Sanz et al 2013
SO201-2-101	58.88	170.68	*N. pachyderma*	Reitdorf et al 2013
SO201-2-85	57.51	170.41	*N. pachyderma*	Reitdorf et al 2013
SO201-2-77	56.33	170.70	*N. pachyderma*	Reitdorf et al 2013
SO201-2-12	53.99	162.36	*N. pachyderma*	Reitdorf et al 2013
MD01-2416	51.27	167.73	*N. pachyderma*	Gebhardt et al 2008
MD01-2416	51.27	167.73	*G. bulloides*	Gebhardt et al 2008
VINO-GGC37	50.28	167.70	*N. pachyderma*	Keigwin 1998
LV29-114-3	49.34	152.88	*N. pachyderma*	Reitdorf et al 2013
KT90-9_21	42.45	144.32	*G. bulloides*	Oba and Murayama 2004
GH02-1030	42.00	144.00	*G. bulloides*	Sagawa and Ikehara 2008
CH84-14	41.44	142.33	*G. bulloides*	Labeyrie 1996
CH84-04	36.46	142.13	*G. bulloides*	Labeyrie 1996
MD01-2420	36.07	141.82	*G. bulloides*	Sagawa et al 2006
MD01-2421	36.02	141.78	*G. bulloides*	Oba and Murayama 2004
KY07_04_01	31.64	128.94	*G. ruber*	Kubota et al 2010
A7	27.82	126.98	*G. ruber*	Sun et al 2005
ODP184-1145	19.58	117.63	*G. ruber*	Oppo and Sun 2005

Additional References

Boyer, T.P., Antonov, J.I., Baranova, O.K., Coleman, C., Garcia, H.E., Grodsky, A., John- son, D.R., Locarnini, R.A., Mishonov, A.V., O'Brien, T.D., Paver, C.R., Reagan, J.R., Seidov, D., Smolyar, I.V., Zweng, M.M., 2013. World Ocean Database 2013. In: Levitus, Sydney (Ed.), Alexey Mishonov (Technical Ed.), NOAA Atlas NESDIS, vol. 72. 209 pp.

Evans D., Wade B. S., Henehan M., Erez J. and Müller W. (2016) Revisiting carbonate chemistry controls on planktic foraminifera Mg / Ca: Implications for sea surface temperature and hydrology shifts over the Paleocene-Eocene Thermal Maximum and Eocene-Oligocene transition. Clim. Past 12.

Gebhardt, H. et al., Paleonutrient and productivity records from the subarctic North Pacific for Pleistocene glacial terminations I to V. Paleoceanography 23, PA4212 (2008).

Gray, W. R., Weldeab, S., Lea, D. W., Rosenthal, Y., Gruber, N., Donner, B. and Fischer, G. (2018b) The effects of temperature, salinity, and the carbonate system on Mg/Ca in Globigerinoides ruber (white): A global sediment trap calibration. Earth Planet. Sci. Lett. 482, 607–620.

Gray, W.R. and Evans, D. (2019) Nonthermal influences on Mg/Ca in planktonic foraminifera: A review of culture studies and application to the last glacial maximum. Paleoceanography and Paleoclimatology, 34. https://doi.org/10.1029/2018PA003517

Harada, N. Ahagon, N., Uchida, M. (2004) Northward and southward migrations of frontal zones during the past 40 kyr in the Kuroshio-Oyashio transition area. Geochemistry, doi:10.1029/2004GC000740/pdf.

Harada, N. (2006) Rapid fluctuation of alkenone temperature in the southwestern Okhotsk Sea during the past 120 ky. Global and Planetary Change. 53, 29–46.

Harada, N., Sato, M., Sakamoto, T. (2008) Freshwater impacts recorded in tetraunsaturated alkenones and alkenone sea surface temperatures from the Okhotsk Sea across millennial-scale cycles. Paleoceanography. 23, PA3201.

Harada, N., Sato, M., Sakamoto, T. (2008) Freshwater impacts recorded in tetraunsaturated alkenones and alkenone sea surface temperatures from the Okhotsk Sea across millennial-scale cycles. Paleoceanography. 23, PA3201.

Hendy, I. L., Kennett, J. P., Roark, E. B., Ingram, B. L., (2002) Apparent synchroneity of submillenial scale climate events between Greenland and Santa Barbara Basin, California from 30-10 ka. Quaternary Science Reviews 21, 1167-1184.

Herbert, D. et al. (2001) Collapse of the California Current During Glacial Maxima Linked to Climate Change on Land. Science. 293, 71–76.

Hill, T.M., J.P. Kennett, D.K. Pak, R.J. Behl, C. Robert, and L. Beaufort. 2006.Pre-Bolling warming in Santa Barbara Basin, California: surface and intermediate water records of early deglacial warmth. Quaternary Science Reviews 25, pp. 2835–2845, doi:10.1016/j.quascirev.2006.03.012

Hönisch B., Allen K. a., Lea D. W., Spero H. J., Eggins S. M., Arbuszewski J., deMenocal P., Rosenthal Y., Russell A. D. and Elderfield H. (2013) The influence of salinity on Mg/Ca in planktic foraminifers – Evidence from cultures, core-top sediments and complementary δ18O. Geochim. Cosmochim. Acta 121, 196–213.

Inagaki, M., Yamamoto, M., Igarashi, Y., Ikehara, K. (2009) Biomarker records from core GH02-1030 off Tokachi in the northwestern Pacific over the last 23,000 years: Environmental changes during the last deglaciation. Journal of Oceanography. 65, 847–858.

Isono, D. et al. (2009) The 1500-year climate oscillation in the midlatitude North Pacific during the Holocene. Geology. 37, 591–594.

Kisakürek, B., Eisenhauer, A., Böhm, F., Garbe-Schönberg, D., Erez, J., 2008. Controls on shell Mg/Ca and Sr/Ca in cultured planktonic foraminiferan, Globigerinoides ruber (white). Earth Planet. Sci. Lett. 273, 260–269. https://doi.org/10.1016/ j.epsl.2008.06.026.

Kubota, Y., K. Kimoto, R. Tada, H. Oda, Y. Yokoyama, and H. Matsuzaki (2010), Variations of East Asian summer monsoon since the last deglaciation based on Mg/Ca and oxygen isotope of planktic foraminifera in the northern East China Sea, Paleoceanography, 25, PA4205, doi:10.1029/2009PA001891.

Labeyrie, L. 1996. Quaternary paleoceanography: unpublished stable isotope records. IGBP PAGES/World Data Center for Paleoclimatology Data Contribution Series #1996-036. NOAA/NGDC Paleoclimatology Program, Boulder. Colorado, USA.

Lea D. W., Mashiotta T. A. and Spero H. J. (1999) Controls on magnesium and strontium uptake in planktonic foraminifera determined by live culturing. Geochim. Cosmochim. Acta 63, 2369–2379.

Maeda, L., H. Kawahata and M. Noharta (2002): Fluctuation of biogenic and abiogenic sedimentation on the Shatsky Rise in the western north Pacific during the late Quaternary. Marine Geology 189, 197-214.

Minoshima, K., H. Kawahata, K. Ikehara (2007) Changes in biological production in the mixed water region (MWR) of the northwestern North Pacific during the last 27 kyr. Palaeogeography, Palaeoclimatology, Palaeoecology. 254, 430–447.

Mortyn, P. G., Thunell, R. C., Anderson, D. M., Stott, L. D., Le, J. (1996) Sea surface temperature changesin the Southern California Borderlands during the last glacial-interglacial cycle. Paleoceanography 11, 415-430.

Narita, H., M. Sato, S. Tsunogai, M. Maruyama, M. Ikehara, T. Nkatsuka, M. Wakatsuchi, N. Harada and U. Ujiie (2002): Biogenic opal indicating less productive northwestern North Pacific during glacial stages. Geophys. Res. Lett., 29(15), 22-1 to 22-4.

Oba, T., Murayama, M. (2004) Sea-surface temperature and salinity changes in the northwest Pacific since the Last Glacial Maximum. Journal of Quaternary Science 19, 335-346.

Oppo, D. W., and Y. Sun (2005) Amplitude and timing of sea surface temperature change in the northern South China Sea: Dynamic link to the East Asian monsoon. Geology 33, 785–788.

Pak, D. K., D. W. Lea, and J. P. Kennett (2012) Millennial scale changes in sea surface temperature and ocean circulation in the northeast Pacific, 10–60 kyr BP, Paleoceanography 27, PA1212, doi:10.1029/2011PA002238.

Peltier, W. R. (2004). Global glacial isostasy and the surface of the Ice-Age Earth: The ICE-5G (VM2) model and GRACE. Annual Review of Earth and Planetary Sciences, 32(1), 111–149. https://doi.org/10.1146/annurev.earth.32.082503.144359

Praetorius, S. K., Mix, A. C. (2014) Synchronization of North Pacific and Greenland climates preceded abrupt deglacial warming. Science 345, 444. DOI: 10.1126/science.1252000.

Prahl, F. G., L. A. Muehlhausen, and D. L. Zahnle (1988), Further evaluation of long-chain alkenones as indicators of paleoceanographic conditions, Geochim. Cosmochim. Acta 52, 2303–2310.

Reimer, P. J. et al. (2013) IntCal13 and Marine13 radiocarbon age calibration curves 0-50,000 years cal BP. Radiocarbon 55, 1869–1887.

Riethdorf, J.-R., Max, L., Nürnberg, D., Lembke-Jene, L., Tiedemann, R. (2013) Deglacial development of (sub) sea surface temperature and salinity in the subarctic northwest Pacific: Implications for upper-ocean stratification. Paleoceanography. 28, 91–104.

Rodríguez Sanz, L., Mortyn, P. G., Herguera, J. C., Zahn, R. (2013) Hydrographic changes in the tropical and extratropical Pacific during the last deglaciation. Paleoceanography. 28, 529–538.

Russell A. D., Hönisch B., Spero H. J. and Lea D. W. (2004) Effects of seawater carbonate ion concentration and temperature on shell U, Mg, and Sr in cultured planktonic foraminifera. Geochim. Cosmochim. Acta 68, 4347–4361.

Sagawa, T., Toyoda, K., Oba, T. (2006) Sea surface temperature record off central Japan since the Last Glacial Maximum using planktonic foraminiferal Mg/Ca thermometry.

Sagawa, T., Ikehara, K. (2008) Intermediate water ventilation change in the subarctic northwest Pacific during the last deglaciation. Geophysical Research Letters 35, L24702, doi:10.1029/2008GL035133.

Seki, O., et al. (2004)Reconstruction of paleoproductivity in the Sea of Okhotsk over the last 30 kyr. Paleoceanography. 19, PA1016.

Singarayer, J.S., Valdes, P.J., Friedlingstein, P., Nelson, S., Beerling, D.J., 2011. Late Holocene methane rise caused by orbitally controlled increase in tropical sources. Nature 470, 8285. https://doi.org/10.1038/nature09739

Taylor, B.J., Rae, J.W.B., Gray, W.R., Darling, K.F., Burke, A., Gersonde, R., Abelman, A., Maier, E., Esper, O., Ziveri, P. (2018) Distribution and ecology of planktic foraminifera in the North Pacific: Implications for paleo-reconstructions. Quaternary Science Reviews 191, 256-274.

Taylor, M. A., Hendy, I. L., Pak, D. K. (2014) Deglacial ocean warming and marine margin retreat of the Cordilleran Ice Sheet in the North Pacific Ocean. Earth and Planetary Science Letters. 403, 89–98 (2014).

Tierney J. E. and Tingley M. P. (2018) BAYSPLINE: A New Calibration for the Alkenone Paleothermometer. Paleoceanogr. Paleoclimatology 33, 281–301.

Yamamoto, M., Oba, T., Shimamune, J., Ueshima, T. (2004) Orbital-scale anti-phase variation of sea surface temperature in mid-latitude North Pacific margins during the last 145,000 years. Geophysical Research Letters. 31, L16311.

Zahn, R., Pedersen, T. F., Bornhold, B. D., Mix, A. C. (1991) Watermass conversion in the glacial subarctic Pacific (54°N, 148°W): physical constraints and the benthic-planktonic stable isotope record. Paleoceanography 6, 543-560.